Received: 21 March 2022 | Revised: 26 July 2022 | Accepted: 2 August 2022

DOI: 10.1002/cne.25398

RESEARCH ARTICLE

JCN RESEARCH IN SYSTEMS NEUROSCIENCE THE JOURNAL OF COMPARATIVE NEUROLOGY WILEY

Analysis of the distribution of vagal afferent projections from different peripheral organs to the nucleus of the solitary tract in rats

Jaspreet K. Bassi[1] | Angela A. Connelly[1] | Andrew G. Butler[1] | Yehe Liu[2] | Anahita Ghanbari[1,3] | David G. S. Farmer[1] | Michael W. Jenkins[2] | Mariana R. Melo[1] | Stuart J. McDougall[4] | Andrew M. Allen[1,4]

[1]Department of Anatomy and Physiology, The University of Melbourne, Parkville, Victoria, Australia

[2]Department of Biomedical Engineering, Case Western Reserve University, Cleveland, Ohio, USA

[3]Department of Queensland Brain Institute, The University of Queensland, St Lucia, Queensland, Australia

[4]Department of Florey Institute of Neuroscience and Mental Health, The University of Melbourne, Parkville, Victoria, Australia

Correspondence
Stuart J. McDougall, Florey Institute of Neuroscience and Mental Health, The University of Melbourne, Parkville, Victoria 3010, Australia.
Email: stuart.mcdougall@florey.edu.au

Andrew M. Allen, Department of Anatomy and Physiology, The University of Melbourne, Parkville, Victoria 3010, Australia.
Email: a.allen@unimelb.edu.au

Funding information
National Health and Medical Research Council, Grant/Award Numbers: 1156727, 1163039; Australian Research Council, Grant/Award Number: DP210102546

Abstract

Anatomical tracing studies examining the vagal system can conflate details of sensory afferent and motor efferent neurons. Here, we used a serotype of adeno-associated virus that transports retrogradely and exhibits selective tropism for vagal afferents, to map their soma location and central termination sites within the nucleus of the solitary tract (NTS). We examined the vagal sensory afferents innervating the trachea, duodenum, stomach, or heart, and in some animals, from two organs concurrently. We observed no obvious somatotopy in the somata distribution within the nodose ganglion. The central termination patterns of afferents from different organs within the NTS overlap substantially. Convergence of vagal afferent inputs from different organs onto single NTS neurons is observed. Abdominal and thoracic afferents terminate throughout the NTS, including in the rostral NTS, where the 7th cranial nerve inputs are known to synapse. To address whether the axonal labeling produced by viral transduction is so widespread because it fills axons traveling to their targets, and not just terminal fields, we labeled pre and postsynaptic elements of vagal afferents in the NTS . Vagal afferents form multiple putative synapses as they course through the NTS, with each vagal afferent neuron distributing sensory signals to multiple second-order NTS neurons. We observe little selectivity between vagal afferents from different visceral targets and NTS neurons with common neurochemical phenotypes, with afferents from different organs making close appositions with the same NTS neuron. We conclude that specific viscerosensory information is distributed widely within the NTS and that the coding of this input is probably determined by the intrinsic properties and projections of the second-order neuron.

KEYWORDS
viscerosensory afferent, dorsal motor nucleus of vagus, area postrema, stomach, duodenum, heart, trachea

1 | INTRODUCTION

The two main groups of visceral afferents that convey sensory and interoceptive information from the viscera to the brain follow either a spinal dorsal root pathway or a vagus nerve pathway. The vagal afferents are pseudo-unipolar neurons whose cell bodies reside in the nodose (NDG) and jugular (JG) ganglia, at the base of the skull, and whose central axons synapse predominantly in the brainstem nucleus of the solitary tract (NTS). The peripheral terminal endings express various mechano-, chemo-, baro-, osmo-, and thermo-sensory receptors in the organs of the gustatory, gastrointestinal, cardiovascular, and respiratory systems. The sensory information is received in the NTS before being integrated and relayed to other medullary as well as higher brain centers. This viscerosensory and interoceptive information generates appropriate motor outputs necessary to maintain and regulate bodily homeostasis, protection, and emotional state via autonomic, endocrine, and behavioral outputs. Disruptions and failures of the viscerosensory network during development or adult life can lead to various morbidities, including obesity, hypertension, asthma, and/or mortality. Therefore, understanding the organization of vagal sensory afferent neuroanatomy, terminal distribution, and signal transmission, both peripherally and centrally, is crucial to deciphering brain function in healthy and disease states.

Examples such as the whisker barrel cortex, with the exquisite preservation of peripheral anatomical organization into the central sensory receptive field, typify our view of the organization of sensory input to the brain (Adibi, 2019). In contrast, the visceral sensory input to the NTS seems to follow less obvious organizational principles. Anatomical tracing studies, using conventional dyes and retrograde viral tracers injected into organs, have not provided a cohesive picture of a somatotopic distribution of the vagal afferent system, either at the level of the sensory cell bodies in the NDG–JG complex (Altschuler, Bao, Bieger, Hopkins, & Miselis, 1989; L. Bai et al., 2019; Muller et al., 2020; Zhong, Christianson, Davis, & Bielefeldt, 2008), or within the NTS (Altschuler et al., 1989; Corbett, Sinfield, McWilliam, Deuchars, & Batten, 2005; Fryscak, Zenker, & Kantner, 1984; Han et al., 2018; McGovern et al., 2015; Shapiro & Miselis, 1985). Attempts to understand the organization of the NTS, based upon physiological and molecular techniques that dissect vagal afferents into diverse molecular and functional subtypes, have revealed a modality-based organization of vagal cell bodies and their terminal afferents (Andresen & Paton, 2011; Mazzone & Undem, 2016; Wang, de Lartigue, & Page, 2020; Zhao et al., 2022). However, substantial overlap exists between the inputs from different organs or modalities. This may reflect that afferents from different organs, conveying similar sensory modality information, could converge at specific subregions of the NTS. Yet even this organizational principal is loose, with studies mapping the trajectory of defined vagal afferents showing that they traverse, and exhibit synaptic boutons in, NTS subnuclei over a long rostro-caudal distance (Kalia & Richter, 1988). Furthermore, integration and modulation of afferent inputs can occur at multiple levels in the network, including presynaptically; at the first site of synapse with a second-order neuron; via convergent inputs to single NTS neurons; or along various poly-synaptic routes within the NTS involving interneurons or extrinsic inputs (Bailey, Hermes, Andresen, & Aicher, 2006; Mifflin, 1996; Mifflin & Felder, 1990). In recent years, the introduction of molecular genetics, combined with the use of anterograde, retrograde, and transsynaptic viral vectors, has enabled an understanding of modality or phenotypic organization of visceral afferents (Borgmann et al., 2021; Han et al., 2018; Kim et al., 2020; Kupari, Haring, Agirre, Castelo-Branco, & Ernfors, 2019; Prescott, Umans, Williams, Brust, & Liberles, 2020). Yet, these techniques have not effectively unraveled the central organization of their inputs. Some evidence indicates that the second-order neurons in the NTS are arranged in clusters, based on convergence of a specific afferent subtype and/or output to higher brain targets (Saper, 2002), but such clusters consist of heterogeneous neuronal populations (de Lartigue, 2014). Fos-based studies have linked stimulation of specific afferent subtypes to specific, phenotypically defined NTS populations; however the distributions are broad and overlapping, and not confined by subnuclear NTS boundaries (Y. Bai et al., 2019; Chan & Sawchenko, 1994; J. Chen et al., 2020). Finally, while there is evidence of parallel and segregated ascending projections of NTS neurons to viscerosensory thalamic and cortical regions based on functional modality (Cechetto, 1987; Gaykema et al., 2009), convergence of these inputs have also been reported (Hanamori, Kunitake, Kato, & Kannan, 1998). At face value, it appears that the visceral sensory system does not follow the obvious hard-wired, labeled line model of somato-, and other sensory systems, and this poses technical challenges to its understanding.

In this article, we mapped the central fields of vagal afferent axons in the NTS by injecting serotypes of adeno-associated viruses (AAV) that transport retrogradely (AAVrg) (Tervo et al., 2016) into their peripheral terminals. The AAVrg did not transduce vagal efferent motor neurons, whose dendrites extend into the NTS and can hamper the identification of vagal afferent projections. This advantage allowed us to label and quantify putative synaptic terminals and compare the close appositions of organ-specific vagal afferent axons with neurochemically defined second-order NTS neurons within the dorsal vagal complex. This approach maps the trajectory of vagal afferent neurons in the NTS, and their putative synapses as they course through the nucleus.

2 | MATERIALS AND METHODS

2.1 | General

All experiments were performed in accordance with the National Health & Medical Research Council of Australia guidelines as outlined in the 2004 Australian code of practice for the Care and Use of Animals for Scientific Purposes and 2008 Guidelines to Promote the Wellbeing of Animals Used for Scientific Purposes. All animal experiments were approved by the University of Melbourne Animal Ethics Committee (Approval Number: 1613875, 1915005). All transgenic experiments were approved by the University of Melbourne Biosafety Committee

(Approval Number: 2018/039) and certified by the Office of the Gene Technology Regulator.

2.2 | Animals

All experiments were performed in male Sprague–Dawley rats (200–400 g) that were bred and housed in the Biological Resources Facility of the University of Melbourne. For this study, we used a total of 25 rats, three of which received viral injections in one organ, 11 viral injections in two organs, and 11 viral injections in the stomach fundus and the NDG (Table 1). Data described in the manuscript are based upon detailed observations in three representative rats for each condition. Animals were maintained on a 12 h light:dark cycle (06:30 to 18:30) at constant ambient temperature (22 ± 1°C), with ad libitum access to standard rat chow and water. Prior to stomach and duodenum surgeries, animals were food-deprived overnight and returned to standard diet postsurgery.

2.3 | Viruses

For organ-specific vagal sensory afferent labeling, we used AAVrg (Tervo et al., 2016) expressing either green fluorescent protein (GFP) or tandem dimer tomato (tdTomato) under the control of the ubiquitous cytomegalovirus/chicken ß-actin promoter (CAG). These viruses were generated by the Boyden laboratory and purchased from AddGene (Watertown, MA, USA; AddGene viral preparations: AAVrg-TdTomato, RRID: Addgene_59462 (1.32×10^{13} GC/ml) and AAVrg-GFP, RRID: Addgene_37825 (1.0×10^{13} GC/ml)). To assess putative synaptic input from vagal sensory afferent projecting into the NTS, we used an AAV expressing the fluorophore GFP fused to Cre recombinase (Cre), under the control of the human synapsin 1 (hSyn1) promoter packaged in a serotype 9 capsid. This virus was generated by the Wilson laboratory and purchased from AddGene (AAV9-hSyn.HI.eGFP-Cre.WPRE.SV40, RRID: Addgene_105540; 5.5×10^{13} GC/ml). This was combined with injection into the NDG of an AAVDJ pseudotyped virus with a Cre-dependent bicistronic vector expressing GFP and synaptophysin fused to mRuby separated by P2A, under the control of the human synapsin 1 promoter (AAVDJ-hSyn-FLEX-mGFP-2A-Synaptophysin-mRuby). This virus was purchased from the Neuroscience Gene Vector and Virus Core, Stanford University, Stanford, CA, USA (GVVC-AAV-100; 6.42×10^{12} GC/ml). To aid the visualization of the site and spread of injectate, 0.2 μl of a 1% solution of Fast Green (Sigma–Aldrich, North Ryde, NSW, Australia) was added to 5 μl of the virus.

To label afferents from the stomach for putative synapse counts, we used either the AAVrg-GFP virus or a bicistronic vector expressing the fluorophore mCherry and Cre recombinase (Cre) separated by an internal ribosome entry site (IRES), under the control of the elongation factor 1α (EF1a) promoter also packaged in AAVrg. This virus was generated by the Deisseroth laboratory and purchased from AddGene (AAVrg-Ef1a-mCherry-IRES-Cre, RRID: Addgene_55632; 8.0×10^{12} GC/ml).

2.4 | General surgical procedures

Isoflurane (Lyppard, Keysborough, VIC, Australia) was delivered for anesthesia during surgical procedures using a digital vaporizer (Somnosuite®; Kent Scientific Corporation, Torrington, CT, USA). For NDG, stomach, and duodenum injections, anesthesia was induced by placing rats in a sealed box containing 5% isoflurane in 100% oxygen and then maintained by inhalation through a nose cone, at approximately 2% isoflurane in 100% oxygen, during the surgery. For heart and trachea injections, animals were deeply anesthetized by inhalation of isoflurane in an induction box followed by injection of a mixture of ketamine (60 mg/kg, i.m.; Lyppard) and medetomidine (250 μg/kg, i.m.; Lyppard). In all cases, a stable surgical plane of anesthesia was assessed by loss of the pedal withdrawal and corneal reflexes. Analgesia (meloxicam, 1 mg/kg, s.c.; Metacam, Lyppard) was administered prior to surgery. The surgical field was shaved, and the incision site was disinfected with 80% (v/v) ethanol, 2% (w/v) chlorohexidine gluconate in 70% (v/v) ethanol (Livingstone, Mascot, NSW, Australia), and betadine antiseptic solution. Lubricating eye ointment (Polyvisc®; Alcon Laboratories, Macquarie Park, NSW, Australia) was applied over the eyes to prevent dehydration during the surgery. The rats were placed on a heating pad lined with a sterile drape and covered with a clear sterile drape. Body temperature was maintained between 37 and 38°C for the duration of surgery (ThermoStar temperature controller; RWD Life Science Co, Shenzhen, Guangdong, China). At the end of the surgery, internal and external incision sites were closed with absorbable 4/0 sutures (Surgicryl® PGA sutures; SMI, St. Vith, Belgium) and warmed Hartmann's solution (1–2 ml i.p.; Baxter Healthcare, Old Toongabbie, NSW, Australia) administered. Ketamine-induced anesthesia was reversed with atipamezole (1 mg/kg, i.m.; Antisedan, Lyppard). The animals were placed on a heat mat until fully recovered from anesthesia and then returned to their standard cage. Animals were housed singly for 24 h postsurgery and then rehoused with littermates. The rats were provided with soft, flavored baby oatmeal for 48 h postsurgery, along with standard rat chow and water to assist recovery. During the recovery period, the rats were monitored for bodyweight, coat condition, general responsiveness and activity, wound healing, and signs of infection.

2.5 | NDG injections

For NDG injections ($n = 11$), the animals were placed supine. A midline incision was made between the mandible and clavicle. The platysma muscle, salivary glands, and lymph nodes were gently retracted to expose the sternohyoid and omohyoid muscles. These muscles were separated and retracted along with the trachea to expose the vagus nerve alongside the common carotid artery. The digastric muscle was retracted laterally to expose the NDG. The connections of the superior laryngeal nerve and glossopharyngeal nerve to the vagus nerve were defined as the posterior and anterior borders of the NDG respectively. Injections were made within these borders. A 30 G needle was used to

TABLE 1 Experimental animal details. Summary table of all experimental animals used in the study, including virus and target injection site details; counts of labeled vagal afferent cells in left (L-NDG) and right (R-NDG) ganglia (^ indicates sectioned and * indicates cleared NDG); presence (Y) or absence (N) of labeled cell bodies in jugular ganglia (JG) and labeled axons in superior laryngeal nerve (SLN) and NTS; number of colabeled NDG cells in animals receiving dual injections of either AAVrg-tdT (tdTomato) or AAVrg-GFP (green fluorescence protein) in two different organ targets; and animals used for data analysis and/or figures

Animal ID	viral tracer	Target 1	L-NDG cell #	R-NDG cell #	JG cells	SLN axons	NTS axons	Viral tracer	Target 2	L-NDG cell #	R-NDG cell #	JG cells	SLN axons	Colabeled NDG cell#	NTS axons	Figure #
End organ afferent labeling/NDG cell distribution and counts/NTS afferent maps/close appositions																
RAT1	AAVrg-**tdTomato**	Prox. Duodenum	2^	1^	N	N	Y	AAVrg-**GFP**	Fundus	8^	5^	N	N	1	Y	NDG#, 3, 4, 7, 8, 9
RAT2	AAVrg-**tdTomato**	Prox. Duodenum	4^	2*	N	N	Y	AAVrg-**GFP**	Fundus	35^	79*	N	N	1	Y	NDG#, 1, 2, 3, 4, 5, 6, 9, 11
RAT3	AAVrg-**tdTomato**	Prox. Duodenum	8*	9*	N	N	Y	AAVrg-**GFP**	Fundus	59*	97*	N	N	0	Y	NDG#, 2, 4, 6, 8, 10
RAT4	AAVrg-**tdTomato**	Fundus	141^	141^	N	N	Y									NDG#, 1, 4
RAT5	AAVrg-**tdTomato**	Fundus	281*	235*	N	N	Y	AAVrg-**GFP**	Prox. Duodenum	0*	0*	N	N	0	N	NDG# 2, 4
RAT6	AAVrg-**tdTomato**	Fundus	234*	112*	N	N	Y	AAVrg-**GFP**	Prox. Duodenum	0*	0*	N	N	0	N	NDG#, 4
RAT7	AAVrg-**tdTomato**	Prox. Trachea	18*	34*	N	N	Y	AAVrg-**GFP**	Cardiac Fat Pad	47*	63*	N	N	7	Y	NDG#, 3, 4, 5, 6, 8, 9
RAT8	AAVrg-**tdTomato**	Cardiac Fat Pad	80^	121*	N	N	Y	AAVrg-**GFP**	Prox. Trachea	24^	49*	N	N	0	Y	NDG#, 1, 2, 4, 6, 8, 11
RAT9	AAVrg-**tdTomato**	Prox. Trachea	2*	6*	N	Y	Y	AAVrg-**GFP**	Cardiac Fat Pad	23*	39*	N	Y	0	Y	NDG#, 1, 2, 4, 9
RAT18	AAVrg-**GFP**	Cardiac Fat Pad	10*	n.e.	N	Y	Y	AAVrg-**tdTomato**	Prox. Trachea	40*	n.e.	N	Y	1	Y	3,8
Putative synapse counts in NTS																
RAT12	AAVrg-**mCherry**-IRES-cre	fundus	0^	2^	N	N	Y	AAV-DIO-**YFP**	NDG	0^	0^				N	13
RAT13	AAVrg-**mCherry**-IRES-cre	fundus	4^	0^	N	N	Y	AAV-DIO-**YFP**	NDG	0^	0^				N	13
RAT14	AAVrg-**GFP**	fundus	7^	20	N	N	Y									13
Putative synapse distribution in NTS																
RAT15	AAV9-cre**GFP**	fundus	n.e.	n.e.			Y	AAV-Flex-**GFP**-P2A-**Syn-mRuby**	NDG	n.e.	n.e.				Y	12

(Continues)

TABLE 1 (Continued)

Animal ID	viral tracer	Target 1	L-NDG cell #	R-NDG cell #	JG cells	SLN axons	NTS axons	Viral tracer	Target 2	L-NDG cell #	R-NDG cell #	JG cells	SLN axons	Colabeled NDG cell#	NTS axons	Figure #
RAT16	AAV9-cre**GFP**	fundus	n.e.	n.e.			Y	AAV-Flex-**GFP**-P2A-**Syn-mRuby**	NDG	n.e.	n.e.				Y	12
Animals not used for figures or data analysis																
RAT10	AAVrg-**tdTomato**	Cardiac Fat Pad	140*	44^	Y	Y	Y	AAVrg-GFP	Prox. Trachea	0*	0^	N	N	0	N	
RAT11	AAVrg-**tdTomato**	Cardiac Fat Pad	171*	167*	Y	Y	Y	AAVrg-GFP	Prox. Trachea	0*	0*	N	N	0	N	
RAT17	AAV9-cre**GFP**	fundus	n.e.	n.e.			Y	AAV-Flex-**GFP**-P2A-**Syn-mRuby**	NDG	n.e.	n.e.				Y	
RAT19	AAVrg-**mCherry**-IRES-cre	fundus	4*	2^			Y	AAV-DIO-**GFP**	NDG	0*	0^				N	
RAT20	AAVrg-**mCherry**-IRES-cre	fundus	5*	1^			Y	AAV-DIO-**GFP**	NDG	0*	0^				N	
RAT21	AAVrg-**mCherry**-IRES-cre	fundus	n.e.	n.e.			Y	AAV-DIO-**mCherry**	NDG	n.e.	n.e.				Y	
RAT22	AAVrg-**mCherry**-IRES-cre	fundus	2^	0^			Y	AAV-Flex-**GFP**-P2A-**Syn-mRuby**	NDG	0^	0^				N	
RAT23	AAVrg-**tdTomato**	fundus	20*	28^			Y									
RAT24	AAV9-cre**GFP**	fundus	23^	n.e			Y	AAV-DIO-**GFP**	NDG	1^	n.e				Y	
RAT25	AAVrg-**mCherry**-IRES-cre	fundus	n.e	n.e			Y	AAV-Flex-**GFP**-P2A-**Syn-mRuby**	NDG	n.e	n.e				Y	

puncture the capsule surrounding the NDG to enable the penetration of a pulled borosilicate glass micropipette (1B100F-4; World Precision Instruments, Sarasota County, Florida, USA) containing the viral solution (tip OD 20–30 μm, beveled ~30–45°). The virus was injected into one site, at a total volume of 0.75 to 1 μl, using a picospritzer (Pneumatic PicoPump, PV820, pulse set at 20 psi, 30–40 ms; World Precision Instruments) to inject small volumes (1–5 nl/pulse) at a rate of ~50 nl/min. In rare cases where the virus leaked from the injection site, the leaked virus was rapidly removed using a cotton bud. All NDG injections were performed bilaterally. The skin was closed with sterile sutures and animals allowed to recover as described above. All animals receiving NDG injections also received viral injections in the stomach fundus during the same surgery.

2.6 | Stomach and duodenal injections

For stomach injections ($n = 14$), the rats were placed supine and a midline incision made in the abdominal skin along the linea alba, ~1 cm posterior to xiphisternum. For dual stomach and duodenum injections ($n = 6$), the incision was extended posteriorly. The abdominal muscle layer was cut to expose the peritoneal cavity, and the surgical opening was lined with sterile gauze soaked in sterile saline. The liver was gently retracted, using cotton tips moistened with saline, to expose the stomach. The stomach fundus was exteriorized, placed on the moistened gauze, and continuously bathed in warm Hartmann's solution throughout the surgery. The virus was injected, using a picospritzer, from a pulled borosilicate glass pipettes (1B150F-4; World Precision Instruments; tip O.D 50–100 μm, beveled 30–45°). The micropipette tip was angled close to the surface of the stomach. Fifteen to twenty injections (0.5–1 μl/site, total volume 8–10 μl) were made into the serosal layer to cover the entire dorsal and ventral surface of the fundus. After each injection, the tip was held in place for 30 s before withdrawing from the injection site. A slight distension of the wall caused by the injectate indicated a successful injection. Any leaked virus was immediately removed. The stomach surface was rinsed thoroughly with Hartmann's solution at the completion. The duodenum was gently lifted above the peritoneal cavity for injections using a similar approach. An acute angle for pipette insertion was essential to inject the serosal layer and avoid injection into the lumen. The virus was injected into seven to ten sites, with a total volume of 5–7 μl, that were equally spaced along the dorsal surface of the duodenum wall, within 2–3 cm of the pylorus. At the end of the injections, the organs were gently returned to their original positions, and the abdominal muscle layer and the skin were closed with sterile sutures.

2.7 | Heart and trachea injections

Dual heart and trachea injections were performed in six rats, with the heart injections preceding the trachea injections. Animals were anesthetized for surgery as described above. Animals were placed supine on an inclined intubation platform (Kent Scientific Corporation) suspended by suture material hooked around the upper incisors. Animals were intubated by positioning the tongue to the side and inserting a 20 G catheter into the trachea, using an optical fiber light source to guide the catheter through the oropharynx. Animals were carefully removed from the intubation platform and placed supine on heating pad lined with sterile drape. The intubating catheter was connected to a ventilator (Harvard Apparatus Inspira Ventilator, MA, USA; parameters 1 ml/100 g, ~60 breaths/min, 2–5 cmH_2O positive pressure). A midline incision was made to expose the thoracic muscles, and the pectoral and latissimus dorsi muscles were separated to expose the ribs. Purse-string suturing was applied to the thoracic muscles ending with a loose knot. This was tightened and secured with an additional knot at the end of the surgery. The second intercostal space was opened by separating the intercostal muscles, the lungs were moved to the side, and the pericardial sac opened. Using a 50 μl Hamilton syringe attached to a 25 G needle, the virus was injected into two pericardial fat pads located central to the aorta and between the aorta and superior vena cava (1 μl/site for a total volume of 2 μl). A cotton tip was used to remove any leaked virus. The intercostal muscles, thoracic muscles and skin were sutured, and the animals were removed from the ventilator. The animals were allowed to return to normal breathing prior to commencing the trachea surgery. A ventral midline incision was made between the chin and clavicle. The platysma muscle, salivary glands, and lymph nodes were retracted using blunt dissection to expose the sternohyoid muscle. The muscle was separated along the midline and retracted to expose the trachea. Using a 50 μl Hamilton syringe attached to a 25 G needle, the virus was injected into the epithelial layer of the posterior tracheal wall. The needle, angled at 45° to the surface of the trachea, was inserted into the trachea through the annular intercartilaginous ligaments. Injections were made into two to three sites (0.6–1 μl/site) located three to six cartilage rings caudal to the larynx. The skin was sutured, and animals were allowed to recover.

2.8 | Transcardial perfusions and tissue collection

Six weeks postinjection, the animals were deeply anesthetized by inhalation of isoflurane in an induction box and injected with a mixture of ketamine (60 mg/kg) and medetomidine (250 μg/kg) i.m. to induce deep surgical anesthesia. They were then perfused transcardially, with 0.1 M phosphate buffer, followed by 4% formaldehyde (FA) in 0.1 M phosphate buffer, at a rate of ~30 mL/min using a peristaltic pump (Masterflex L/S Drive System, Cole-Parmer, Vernon Hills, Illinois, USA). The brains were removed, postfixed in 4% FA in 0.1 M phosphate buffer for 4 h at room temperature (RT), and then immersed in 20% sucrose at 4°C until processing. The heart, trachea, stomach, and duodenum were removed and postfixed in 4% FA in 0.1 M phosphate buffer overnight at 4°C and immersed in 0.1 M phosphate buffer at 4°C until processing. The thorax and head were postfixed in 4% FA in 0.1 M phosphate buffer overnight and washed several times with in 0.1 M phosphate buffer over the following 24 h, before the NDG were dissected out, along with the distal vagal trunk and the superior laryngeal nerve, to its entry to the posterior lacerated foramen. It was then immersed in 20% sucrose at 4°C until processing.

2.9 | Tissue clearing

Several tissue clearing approaches were used and the most successful applied to particular tissues.

2.9.1 | iDISCO+ clearing

Fixed tracheas were cleared using the iDISCO+ protocol (Renier et al., 2014). Samples were dehydrated with methanol/H_2O series: 20, 40, 60, 80, 100% (v/v) for 1 h each, washed with 100% methanol (1 h) and chilled at 4°C. Samples were treated with 66% dichloromethane (DCM; Sigma–Aldrich–Merck; Cat# 270997) and 33% (v/v) methanol overnight with shaking, washed twice in 100% methanol at RT and chilled at 4°C. Samples were bleached in chilled fresh 5% (v/v) H_2O_2 in methanol overnight at 4°C, then rehydrated with methanol/H_2O series: 80, 60, 40, 20% (v/v), 1× phosphate-buffered saline (PBS); 1 h each at RT. Samples were washed twice in 1× PBS containing 0.2% (v/v) Triton X-100 (PTx0.2) at RT for 1 h, incubated in permeabilization solution (PTx0.2 with 20% (v/v) dimethyl sulfoxide [DMSO], and 0.3 M glycine, 37°C, 1.5 days), and placed in blocking solution (PTx0.2 with 5% (v/v) DMSO and 3% (v/v) horse serum (Invitrogen-Thermo Fisher Scientific, Scoresby, VIC, Australia; Cat# 26050–070)) at 37°C for 2 days. Primary antibody incubation occurred in 1× PBS containing 0.2% (v/v) Tween-20 and 0.01 mg/ml Heparin (Sigma–Aldrich–Merck, Cat# H3393; PTwH) with 5% (v/v) DMSO, and 3% (v/v) horse serum) at 37°C for 3 days. Samples were washed in 4–5 changes of PTwH over the next day, incubated with secondary antibody in PTwH/3% (v/v) horse serum at 37°C for 2.5 days, and washed in PTwH for four to five times until the next day. Samples were then dehydrated in methanol/H_2O series: 20, 40, 60, 80, 100, 100% (v/v); 1 h each at RT then incubated for 3 h, with shaking, in 66% DCM with 33% (v/v) methanol at RT. Samples were further incubated in 100% DCM 15 min twice (with shaking) to wash out the methanol, then incubated in dibenzyl ether (DBE; Sigma–Aldrich–Merck; Cat# 108014) for storage at RT until imaging in ethyl cinnamate (Sigma–Aldrich–Merck; Cat# 112372).

2.9.2 | Adipoclear

Fixed heart samples were cleared via Adipoclear (Chi et al., 2018). Hearts were cut into smaller regions, then washed in 20, 40, 60, 80% (v/v) methanol in 0.1% (v/v) Triton X-100 and 0.3 M glycine, pH 7; B1N buffer), and 100% methanol for 30 min each. Samples were delipidated by washing with 100% DCM for 30 min three times, then 100% methanol for 30 min twice, before rinsing in 80, 60, 40, 20% (v/v) methanol in B1N buffer for 30 min each step. Samples were then washed in B1N for 30 min twice followed by PTwH buffer (1× PBS, 0.1% Triton X-100, 0.05%(v/v) Tween 20, 2 mg/ml heparin) for 1 h twice before further staining procedures. Samples were incubated in primary antibody dilutions in PTwH for 4 days. After primary antibody incubation, samples were washed in PTwH with five changes and overnight, incubated in secondary antibody dilutions in PTxwH for 3 days, and finally washed in five changes of PTwH, and overnight. Samples were then prepared for clearing via dehydration in 25, 50, 75, 100, 100% (v/v) methanol/H_2O series for 30 min at each step at RT. Following dehydration, samples were washed with 100% DCM for 30 min twice, followed by an overnight clearing step in di-benzyl ether. Samples were stored at RT in the dark until imaged in ethyl cinnamate.

2.9.3 | LIMPID clearing

Fixed NDGs were cleared using LIMPID (Liu, Watanabe, Rollins, & Jenkins, 2018). Tissues were washed in 4 parts methanol with 1 part DMSO at RT overnight. An equal volume of 1× PBS was added to the methanol–DMSO mix also containing 10% (v/v) H_2O_2 and washed for 30 min. The samples were washed with 1× PBS, 2 × 30 min. Samples were blocked in 1× PBS with 3% (w/w) bovine serum albumin (BSA; Sigma–Aldrich–Merck; Cat# A7906), 0.01% (w/v) sodium azide, 1% Triton X-100, at 37°C for 4 h, stained with blocking buffer containing primary antibody (37°C, >12 h), and then washed with three changes of blocking buffer (37°C for 2 h each). Secondary antibodies were added to blocking buffer and incubated at 37°C, overnight. Samples were washed in blocking buffer at 37°C for 4 h, then washed twice in 1× PBS at RT for 30 min. The clearing agent, LIMPID-N 1.470 (Lipid-preserving Index Matching for Prolonged Imaging Depth), is prepared as described previously (Liu et al., 2018). Samples were incubated in 1.5 ml of LIMPID, shaken at 37°C overnight. Clearing solution was replaced with fresh LIMPID-N 1.470 for 2 h, then stored in mineral oil at RT, and visualized in mineral oil.

2.10 | Cryostat sectioning

The NDG were embedded and frozen in embedding medium (Tissue-Tek OCT compound; ProSciTech, Thuringowa Central, QLD, Australia) as described previously (Ngo et al., 2020). Four series of sections (16 μm thickness) were cut on a cryostat (HM525, Microm; Thermo Fisher Scientific, Walldorf, Germany) at −20°C, thaw-mounted on gelatin-coated slides and stores at −20°C until processing.

Brainstems were frozen at −20°C, and six series of coronal sections (40 μm thickness) were cut on a cryostat from the emergence of the pyramidal decussation caudally (bregma −15.48 mm) to the emergence of facial nerve rostrally (bregma −10.20 mm). Sections were placed directly into cryoprotectant (0.88 M sucrose, 0.25 mM polyvinyl-pyrrolidone, 4.35 M ethylene glycol, 50 mM sodium phosphate buffer, pH 7.2) in a 24-well plate and stored at −20°C until processing.

2.11 | Immunohistochemistry

2.11.1 | NDG sections

Immunohistochemistry was performed on one of the four series of NDG sections, as previously described in detail (Ngo et al., 2020). Immunostaining was performed to detect GFP or TdTomato, using GFP or dsRed antibody respectively, along with a pan-neuronal

marker, NeuN. Nuclei were stained with 4′,6-diamidine-2-phenylindole dihydrochloride (DAPI; Sigma–Aldrich–Merck, Bayswater, VIC, Australia; 1:50,000; Cat#: D9542).

2.11.2 | Brain sections

Immunohistochemistry was performed one in six series of free-floating brainstem sections as described in detail previously (D. Chen, Bassi, Walther, Thomas, & Allen, 2010; Menuet et al., 2020; Menuet et al., 2017; Sevigny et al., 2012). Immunostaining was used to detect GFP, tdTomato, or mCherry; specific cell markers tyrosine hydroxylase (TH), choline acetyltransferase (ChAT), 11ß-hydroxy-steroid dehydrogenase type 2 (HSD2), glucagon-like peptide 1 (GLP-1) and neurokinin receptor 1 (NK1R); and synaptic protein markers synapsin 1 (SYN1) and postsynaptic density protein 95 (PSD95).

2.11.3 | Antibody characterization

Chicken anti-GFP antiserum (Aves Labs Inc, Davis, CA, USA; Lot: 0511FP12, Cat#: GFP-1010, RRID: AB_2307313, used at 1:5000 for brain sections or at 1:1000 for NDG sections) is raised against recombinant GFP. The manufacturer determined the specificity by western blot analysis and immunohistochemistry using transgenic mice expressing the GFP gene product. The antibody shows labeling only in tissues expressing GFP (Bochorishvili et al., 2014).

Rabbit anti-dsRed antiserum (Takara Bio, Clontech, Australia; Lot: 1805060, Cat#: 632496, RRID: AB_10013483, used at 1:5000 for brain sections or 1:1000 for NDG sections) is raised against DsRed-Express, a variant of *Discosoma sp.* red fluorescent protein and recognizes all other red fluorescent protein variants. The manufacturer determined the specificity by western blot analysis using lysate from untransfected HEK 293 cells and lysates from HEK 293 cells stably expressing DsRed-Express or AcGFP1. A specific band of approximately 30–38 kDa was observed with lysate from cells expressing DsRed-Express. No band in this molecular weight range was detected for the lysates of the untransfected HEK 293 cells or the cells expressing AcGFP1. In our hands, the antibody shows labeling only in tissue injected with viral vectors expressing GFP (Menuet et al., 2020; Menuet et al., 2017; Ngo et al., 2020).

Goat anti-mCherry (Sicgen, Cantanhede, Portugal; Lot: 0040061015, Cat#: AB0040-200, RRID: AB_2333092, used at 1:5000) is a purified recombinant peptide raised against mCherry fluorescent protein and recognizes all other red fluorescent protein variants. The manufacturer determined the specificity in 293HEK cells transfected with cds plasmid and detected a band of 29 kDa by western blot. We observed that this antibody labels tissue injected with viral vectors expressing tdTomato and mCherry expressed by viral vectors and does not recognize GFP (Menuet et al., 2017; Ngo et al., 2020).

Mouse anti-NeuN antiserum (Chemicon-Merck, Bayswater, Australia; Lot: 3248401, Cat#: MAB377, RRID: AB_2298772, used at 1:500) is raised against neuronal nuclear protein. The manufacturer performed routine evaluation of the antiserum by immunohistochemistry on brain tissue and assessed staining and morphology in rat cerebellum. Immunoreactivity is seen as nuclear staining in the neurons in the granular layer. Note that there is no signal detected in the nucleus of Purkinje cells. In western blots, the antibody recognized two to three bands in the 46–48 kDa range and possibly another band at approximately 66 kDa. Moreover, in our hands, the antibody yielded a pattern previously reported (Allen et al., 2008; Menuet et al., 2017).

Human anti-Hu antiserum: (generous gift from Prof. V. Lennon, Mayo Clinic College of Medicine, Minnesota, USA, Cat# Hu, RRID: AB_2314657) This antibody recognizes the Elav family members HuC, HuD, and Hel-N1 neuronal proteins. The antibody has been shown to specifically label neuronal cells (Carter et al., 2017).

Goat anti-ChAT antiserum (Chemicon-Merck; Lot: 3491643, Cat#: AB144P, RRID: AB_2079751, used at 1:1000) raised against human placental enzyme. The manufacturer verified the specificity by western blot analysis using mouse brain lysates and detected a 68–70 kDa band corresponding to the ChAT protein. Moreover, we observed that the antibody yielded a labeling pattern within rat brain tissue sections previously reported in literature (Menuet et al., 2020; Ngo et al., 2020; Sevigny et al., 2012).

Mouse anti-TH antiserum (Merck-Millipore, Bayswater, VIC, Australia; Lot: 3083054, Cat: MAB318, RRID: AB_2201528, used at1:5000) raised against purified rat TH and recognizes an epitope located in the N-terminal region. The manufacturer verified the specificity by western blot analysis using cell line lysates and detecting a 60 kDa band corresponding to the TH protein. In our hands, the antibody yielded labeling pattern in rat brain sections previously reported in literature (D. Chen et al., 2010; Menuet et al., 2020; Ngo et al., 2020; Sevigny et al., 2012).

Sheep anti-rat HSD2 antiserum (Merck-Millipore; Lot: 1979252, Cat#: AB1296, RRID: AB_90575, used at 1:160,000) raised against a recombinant protein generated from nucleotides 385–1204 of the rat HSD2 gene. The antibody staining in rat brain correlates with in situ hybridization studies of HSD2 mRNA localization in the rat brain (Geerling, Kawata, & Loewy, 2006; Shin & Loewy, 2009).

Rabbit anti-GLP-1 (Peninsula Laboratories-BMA Biomedicals, Augst, Switzerland; Lot: A13642, Cat#: T-4363, RRID: AB_518978, used at 1:10,000) is a synthetic 31 amino acid peptide coupled to a carrier protein. The manufacturer has tested and validated this antibody in ELISA against GLP-1 (7–37). In our study, the antibody yielded pattern of labeling in rat brain slices as previously reported (Card et al., 2018; Edwards, Strother, Zheng, & Rinaman, 2019).

Rabbit anti-NK1R antiserum (Sigma–Aldrich–Merck; Lot: 125M4862V, Cat#: S8305, RRID: AB_261562, used at 1:5000) is raised against a synthetic peptide corresponding to the C-terminal of NK1R of rat origin (amino acids 393–407). This sequence is highly conserved in mouse, guinea pig, and human NK1R, but diverges in other tachykinin receptor subtypes NK2R and NK3R. The manufacturer verified the specificity by western blot analysis using whole rat brain lysates and detected a 46 kDa band corresponding to the NK1R protein. Staining of the NK1R band (46 kDa) in immunoblotting was specifically inhibited with NK1R peptide (rat, amino acids 393–407). Immunohistochemical staining in tissue sections of rat brain matched patterns shown in previous studies (Menuet et al., 2020; Menuet et al., 2017).

Rabbit anti-SYN1 antiserum (Invitrogen-Thermo Fisher Scientific; Lot#: 549874A, Cat#: 51–5200, RRID: AB_2533909, used at 1:1000) is raised against purified bovine brain Synapsin 1. The manufacturer determined the specificity by western blot analysis. A 78 kDa band corresponding to Synapsin-1 was detected in whole cell extracts (IMR 32 and PC-12) and tissue extracts of mouse and rat brain but absent in mouse lung and heart lysates. We observed immunohistochemistry staining in rat brain tissue as previously reported (Bertran-Gonzalez, Laurent, Chieng, Christie, & Balleine, 2013; Mahn, Prigge, Ron, Levy, & Yizhar, 2016).

Mouse anti-PSD95 antiserum (Chemicon-Merck; Lot#: 3429638, Cat#: MAB1596, RRID: AB_1679597, used at 1:400) was raised against recombinant rat PSD-95. The manufacturer verified the specificity by immunocytochemistry on PC12 cells and western blot analysis on brain rat, mouse, and bovine tissue extracts, which detected a 100 kDa band corresponding to the PSD-95 protein. We observed immunohistochemistry straining in rat brain tissue as previously reported (Li et al., 2010).

All secondary antibodies were purchased from Jackson ImmunoResearch Laboratories, Inc, West Grove, Pennsylvania, USA, unless stated, and used at either 1:500 (for brain sections) or at 1:200 (for NDG sections). Antibody dilutions and incubation times were optimized to ensure complete penetration of antibodies in the brain sections as described previously (Ngo et al., 2020). The following secondary antibodies were used Alexa488-conjugated donkey anti-chicken (Lot#: 133645, Cat: 703545155, RRID: AB_2340375), Alexa488-conjugated donkey anti-rabbit (Lot#: 127725, Cat: 711545152, RRID: AB_2313584), Alexa488-conjugated donkey anti-mouse (Lot#: 143224, Cat#: 715545151, RRID: AB_2341099), Cy3-conjugated donkey anti-rabbit (Lot#: 133645, Cat: 711165152, RRID: AB_2307443), Cy3-conjugated donkey anti-goat (Lot#: 87377, Cat: 705165003, RRID: AB_2340411), Cy5-conjugated donkey anti-mouse (Lot#: 120906, Cat: 715175151, RRID: AB_2340820), Cy5-conjugated donkey anti-goat (Lot#: 124689, Cat#: 705175147, RRID: AB_2340415), and Cy5-conjugated donkey anti-rabbit (Lot#: 129208, Cat#: 711175152, RRID: AB_2340607). Alexa647-conjugated donkey anti-guinea pig (Lot#:145782, Cat#: 706605148, RRID: AB_2340476), Biotin-SP-conjugated donkey anti-human (Lot#: 155263, Cat#: 709065149, RRID: AB_2340507) and Streptavidin-Marina blue (Lot#: 1893214, Cat#: S11221 were purchased from Invitrogen-Thermo Fisher Scientific.

2.12 | Imaging

Imaging was performed in the Biological and Optical Microscopy Platform at the University of Melbourne.

2.13 | Epifluorescence microscopy

Brain. Low power images were acquired using a Zeiss Axio Imager D1 microscope with a Zeiss AxioCam MR3 camera and EC Plan-NeoFuar 10×/0.3 air objective (Carl-Zeiss, North Ryde, NSW, Australia). Images were captured and visualized with AxioVision v4.8 imaging software. Images were taken in the green (Ex λ493/Em λ517), red (Ex λ548/Em λ561) and far-red (Ex λ650/Em λ673) channels.

NDG. Low-resolution tiled images were captured on Zeiss Axio Imager.M2 microscope with an Apocromat 20×/0.8 air objective (Carl-Zeiss) with a motorized stage using Axiocam 506 mono camera and ZEN 2.6 (blue edition) imaging software. Images were taken in the green (Ex λ493/Em λ517), red (Ex λ548/Em λ561), far-red (Ex λ650/Em λ673), and blue (Ex λ353/Em λ465) channels. To image the entire NDG section, tile scan was performed with 10% overlap between neighboring tiles and image stitched in the Zen software.

2.14 | Confocal microscopy

Brain. Images were captured on Zeiss LSM880 confocal laser scanning microscope with Airyscan detectors (32 GaAsP PMT array) using a Plan-Apochromat 20×/0.8 M27 objective (Carl-Zeiss) and ZEN 2.3 (black edition) imaging software. Excitation light at 488, 561, and 633 nm was supplied by Argon laser (25 mW) and HeNe lasers (2 and 5 mW), respectively. Band-pass filters were used to prevent bleed-through of signals (488 nm: BP 420–480 + BP 495–550; 561 nm: BP 420–480 + BP 495–620; 633 nm: BP 570–620 + LP 645) and images scanned sequentially, frame by frame. Laser power for each channel was set to avoid pixel saturation (occupied half to two-thirds of the detector dynamic range). Airyscan detector calibration was performed prior to image acquisition and rechecked for every new slide. Scan speed was set to maximum, Nyquist rate to 2×, scan average to 1, zoom to 1, gain to 850 and digital gain to 1. Images were taken in Airyscan Fast mode using a bidirectional line scan captured on an 8-bit gray scale. *z*-Stack images were taken with 0.4 μm *z*-intervals, and at least 50% overlap between optical slices obtaining 40–50 images over 15–30 μm thickness. A tile scan was performed, with 10% overlap between neighboring tiles, to image the entire distribution of labeled afferent fibers in the section. Images were 3D Airyscan processed with the Weiner parameter (10^{-f}) and the *f* value (Airyscan filter strength) for all images set to 6 followed by tile stitching in the Zen black software.

Cell appositions. Confocal images were acquired as described above with the following modification. High-resolution images were captured using a Plan-Apochromat 63×/1.4 Oil DIC M27 objective. Immersion oil (Immersol 518F; R.I. 1.518; Carl-Zeiss) with matching refractive index to the mounting medium (Cytoseal 60; R.I. 1.495; ProSciTech) was used. Scan speed adjusted to achieve pixel dwell approximately 1 μs, zoom set to 1.5 and average to 2. Isolated cells and their neurites, contacted by sparse vagal afferents were selected and centered in a field of view 90 × 90 μm. Image size was 2112 × 2112 pixels and voxel dimensions were 0.04 × 0.04 × 0.18 μm in the *x*, *y*, and *z* directions. *z*-Stacks were obtained with 0.18 μm intervals and at least 50% overlap between optical slices obtaining 40–60 images over 8–12 μm thickness.

Putative synapses. Images were captured as described for cell appositions with the following modifications. Zoom was set to 1.8, image size was 1760 × 1760 pixels with field of view 75 × 75 μm and voxel dimensions were 0.04 × 0.04 × 0.12 μm in the *x*, *y*, and *z* directions.

z-Stacks were obtained with 0.12 μm optical slice intervals corresponding to 40–80 images over 6–10 μm thickness. Images were taken from lengths of well isolated continuous axons, at least 50 μm long, from sparsely labeled tissue samples.

2.15 | Lightsheet microscopy

Lightsheet microscopy was performed on an Ultramicroscope II (La vision Biotech, Bielefeld, Germany), using a LaVision (LVMI-Fluor 4×) objective and Biotec Inspector imaging software. Excitation light at 488, 561, and 639 nm was supplied by LASOS Diode and LASOS DPSS lasers (85, 100, and 70 mW) respectively. The camera used was an Andor Neo sCMOS (2560 × 2160 pixels). A 5 μm sheet numerical aperture was used and 100% sheet width, the pixel value did not exceed 60,000. *z*-Stacks were obtained with a 4 μm step size using either a single or dual lightsheet.

2.16 | Image processing and analysis

For publication, images along with their meta data were imported into Image J (v1.53c, 64-bit; Rasband, W.S., U. S. National Institutes of Health, Bethesda, Maryland, USA, https://imagej.nih.gov/ij/, 1997–2018.), using the Bio-format plugin. Images were cropped, and, if required, the entire image was adjusted for brightness and/or contrast and embedded with scale bar. Maximum intensity projections were created from *z*-stack images. Multichannel images were merged. The final images were exported as tiff (RGB) files into the vector graphics editing software, Inkscape (v1.0, 2020), and images resized and assembled into figures.

2.17 | NTS maps

Whilst the distribution of axonal processes was examined in all animals (n = 25), which was found to be consistent among all replicate animals, maps were generated from three representative animals injected in each target organ (n = 9). Brain sections corresponding to seven distinct rostral to caudal levels of NTS were selected based on the distribution of TH immunoreactive neurons and cytoarchitectural landmarks as defined in The Rat Brain in Stereotaxic Coordinates (Paxinos & Watson, 2004). Airyscan processed and stitched images were opened in Image J in 16-bit format and maximum intensity projections were created. The channel containing vagal afferent labeling was selected (in dual labeled tissue, channels were selected and processed individually) and brightness and/or contrast adjusted to maximize the signal and minimize background. Image segmentation was achieved by applying global threshold values (low: 1000–2000; high: 65,535; total range: 0–65,535). The low threshold value was determined manually from the histogram as the value closest to the right lower boundary of the background peak. The selected threshold values usually covered ~0.5% histogram pixels. The resulting binary image was imported into Inkscape software and converted into a vector image using the Trace Bitmap tool (single scan mode, brightness cutoff threshold set to 0.45). The traced bitmap image was overlayed on the corresponding coronal brainstem schematic diagram, using the original fluorescence image as a guide. Traced afferents from each animal and each organ were color coded and combined to form the single or dual NTS distribution maps. Stroke was added (width: 0.182 mm, bevel join) to enhance visualization of the traced afferents in the final figure.

2.18 | Cell appositions

Each optical slice, from a *z*-stack NTS image of a fluorescently labeled cell and fluorophore expressing vagal afferent, was manually examined using the Zen black software to determine close appositions between the cell body or its neurite and the vagal afferent. An overlapping region of the two fluorophores was defined as a putative contact. *z*-Stack images were also resliced in Image J to generate an image along a line drawn across the putative contacts thus creating a single plane "side view" image.

2.19 | NDG cell counts

In sectioned NDG (total six from four rats), transduced cells expressing fluorophore were manually counted in Zen blue software. NDG cells were identified as large ovoid or rounded cells that costained with the pan-neuronal marker, NeuN and with DAPI stained nuclei. Every fourth section (64 μm apart) was counted to avoid double counting. In whole ganglia (total 12 from 7 rats), cells with pseudo-unipolar morphology were counted using IMARIS (v 9.5.1; Bitplane AG, Zurich, Switzerland). Tiff images were imported, and 3D surface rendering was applied to the nodose neurons using the "surfaces" tool. Regions were segmented, and thresholding with a background subtraction diameter of 7.5 μm was used. Split touching objects were selected, with seed point diameter of 10 μm, and a voxels filter for sphericity was used, to generate the automated NDG neuron cell counts. Organ-specific NDG cell counts (n = 3 per organ) were calculated as mean ± standard deviation (*SD*) using GraphPad Prism (version 9.2.0 for Windows 64-bit, GraphPad Software, San Diego, CA, USA).

2.20 | Putative synapse distribution

Animals (n = 4) with stomach-specific vagal afferent axons labeled with mGFP and their putative synaptic terminals labeled with mRuby were examined. Consistent putative synapse distribution patterns were observed in all animals. Airyscan processed and stitched 3D confocal images from one representative animal were opened in Image J in 16-bit format and maximum intensity projections created. The channels were individually selected and the brightness and/or contrast adjusted to maximize signal and minimize background. Fluorescence colors of the vagal afferents and synaptophysin were changed to red and white, respectively, the channels were merged, and the image colors inverted to achieve cyan-colored afferents labeling with

black synaptophysin labeling on a white background. Subregions were selected from five distinct rostral to caudal levels of NTS based on cytoarchitectural landmarks as defined in The Rat Brain in Stereotaxic Coordinates (Paxinos & Watson, 2004).

2.21 | Putative synapse counts

3D high-resolution images (n = 3) containing fluorescently labeled stomach vagal afferents and presynaptic and postsynaptic markers, synapsin 1 and PSD95, respectively, were used to quantify putative synapses based on size and fluorescence intensity measurements indicated below and described by Schatzle and colleagues (Schatzle, Wuttke, Ziegler, & Sonderegger, 2012). Airyscan processed images were opened in Image J in 16-bit format, cropped and brightness and/or contrast were adjusted where required. Tiff images were imported into Imaris, and synapse quantification performed as follows. First, 3D surface rendering was applied to the afferent axon (50 μm) using the "surfaces" tool. To reduce noise, the smooth option was selected and surface area detail level set to 0.0852 μm. Absolute intensity threshold was applied, and surfaces classified with the "number of voxels" filter to remove background. Second, segmentation of the pre- and postsynaptic puncta in the image was achieved by using the "spots" tool. Spots were detected using an estimated diameter of 0.426 μm, and background subtraction applied. Spots were classified using the "quality" threshold filter set to 500. Third, presynaptic spots localized within the axon and postsynaptic spots localized close to the axon were selected by using the "find spots close to surface" MATLAB v3 (MathWorks Inc, Natick, MA, USA) script within Imaris and setting threshold distance to 0.1 and 0.7 μm, respectively. Finally, a putative synapse was defined as a pair of spots, pre- and postsynaptic, that were located within a certain distance. Automated synapse counts were performed using the "colocalize spots" script and setting the maximum allowed distance between spots to 0.4 μm. The threshold distance generated results that were equivalent to results from manual synapse quantification. To quantify putative synaptic contacts with second-order neurons (n = 1), the above protocol was used with the following modifications: 3D surface rendering was applied to neurons, postsynaptic spots were selected based on localization within the neurons by applying "find spots close to surface" threshold distance of 0.1 μm.

3 | RESULTS

3.1 | Organ-specific central vagal afferent distributions

3.1.1 | General observations

We injected AAVrg, that express either red (tdTomato) or green (GFP) fluorescent protein under the control of a pan-neuronal promoter (CAG), into peripheral organs to trace the organ-specific vagal innervation in the brainstem. Fluorophore expression occurred throughout the transduced neuron, enabling examination of the somata and all processes. We observed specific tropism of AAVrg for sensory afferent neurons, with fluorophore expression in the peripheral axon within the organ (Figure 1); the somata in the NDG (Figure 2); and the central axons within the brainstem (Figures 3 and 4). The AAVrg also transduced intrinsic neurons within the stomach and duodenum (Figures 1(a) and 1(b)). We did not observe any transduction of neurons in the area postrema, a circumventricular organ (AP; Figures 3(a) and 3(b), or vagal efferent motor neurons, whose somata are in the dorsal motor nucleus of the vagus (DMV; Figures 3(c) and 3(d)) or the nucleus ambiguus (NAmb; Figure 3(e)), following AAVrg injection into any organ. In this study, we have concentrated on vagal sensory innervation of the brainstem and did not examine transduction of dorsal root ganglion afferents.

The somata of transduced neurons within the NDG, from all injected peripheral organs, showed typical pseudo-unipolar morphology (Figures 2 and 5). Transduced neurons were distributed throughout the rostral–caudal extent of the ganglia without any obvious compartmentalization or somatotopic organization. Labeled afferent axons were observed in the vagal trunk, traversing the ganglia, and within the medulla oblongata. The central terminations from all injected targets were located in the NTS, AP and DMV. The terminals displayed varying degrees of axonal thickness, branching, and numbers of varicosities and boutons.

We observed differences in the labeling efficacy between the viruses used, with AAVrg-CAG-GFP being less efficient than AAVrg-CAG-tdTomato. We cannot determine why alteration of the fluorophore, expressed by an identical plasmid/promoter construct, packaged with the same pseudotype capsid, and produced by the same facility with a similar titre, should result in differential levels of transduction. For example, AAVrg-CAG-GFP injections in duodenum did not label any neurons in 2 out of 2 animals, whereas AAVrg-CAG-tdTomato injections were successful in all attempts (Table 1). Similar differences were observed with injections in the trachea. Furthermore, AAVrg-CAG-GFP tended to transduce fewer NDG cells, and their central and peripheral afferent terminals, compared to AAVrg-CAG-tdTomato (Table 2). To overcome this discrepancy, data comparing the labeling from different organs was derived from injections of AAVrg-CAG-tdTomato. We observed less variability between the vectors for injections in the heart and trachea, so for these organs, data were derived from both vectors with AAVrg-CAG-tdTomato used for two out of three heart injections and for one out of three trachea injections. Whilst we observed variations in the density of labeling with the different vectors, the pattern of afferent axon distribution within NTS subnuclei was consistent between vectors.

3.1.2 | Distribution of vagal afferent axons from single peripheral organs in the NTS

To describe the distribution of axonal labeling within the NTS, for this, and all other target organ injections, the rostral NTS was defined as rostral to the rostral border of the AP (bregma -11.00 to -13.68 mm); the

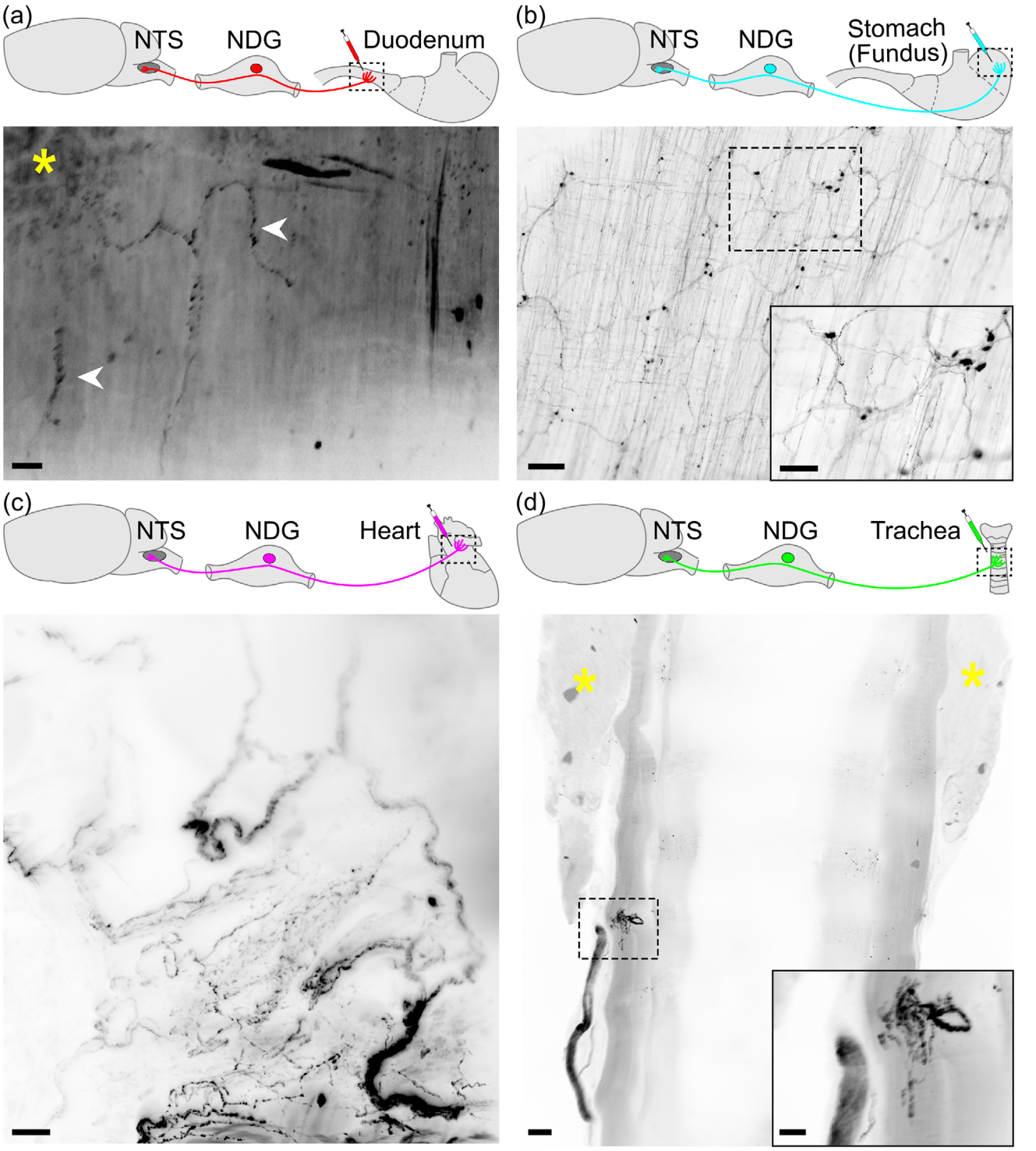

FIGURE 1 Transduced cells and processes in target organs injected with retrograde adeno-associated virus (AAVrg). The schematics show the site of AAVrg injection and the tissue region (dashed box) corresponding to the photomicrograph. (a) Lightsheet photomicrograph (180 μm *z*-stack) of a cleared segment of proximal duodenal wall. Transduced axons are highlighted with white arrowheads. An autofluorescent crypt is highlighted with a yellow asterisk. (b) Epifluorescence photomicrograph of 90.4 × 67.2 μm cleared area of fundus wall showing transduced axons and enteric neurons. A higher magnification of the dashed boxed is shown in the inset. (c) Lightsheet photomicrograph (604 μm *z*-stack) of cleared fat pad tissue from the dorsal surface of the heart showing transduced thick bundles and fine branches of transduced axons. (d) Lightsheet photomicrograph (756 μm *z*-stack) of cleared proximal tracheal wall showing a transduced axonal bundle and fine branches. Autofluorescence in the thyroid glands is highlighted with yellow asterisks. A higher magnification of the dashed boxed is shown in the inset. All images are presented as maximum intensity projections and representative of $n = 3$ per injection site. All scale bars are 100 μm except in (b) and (d) lower magnification scale bar = 200 μm. *Abbreviations*: NTS, nucleus of the solitary tract; NDG, nodose ganglia

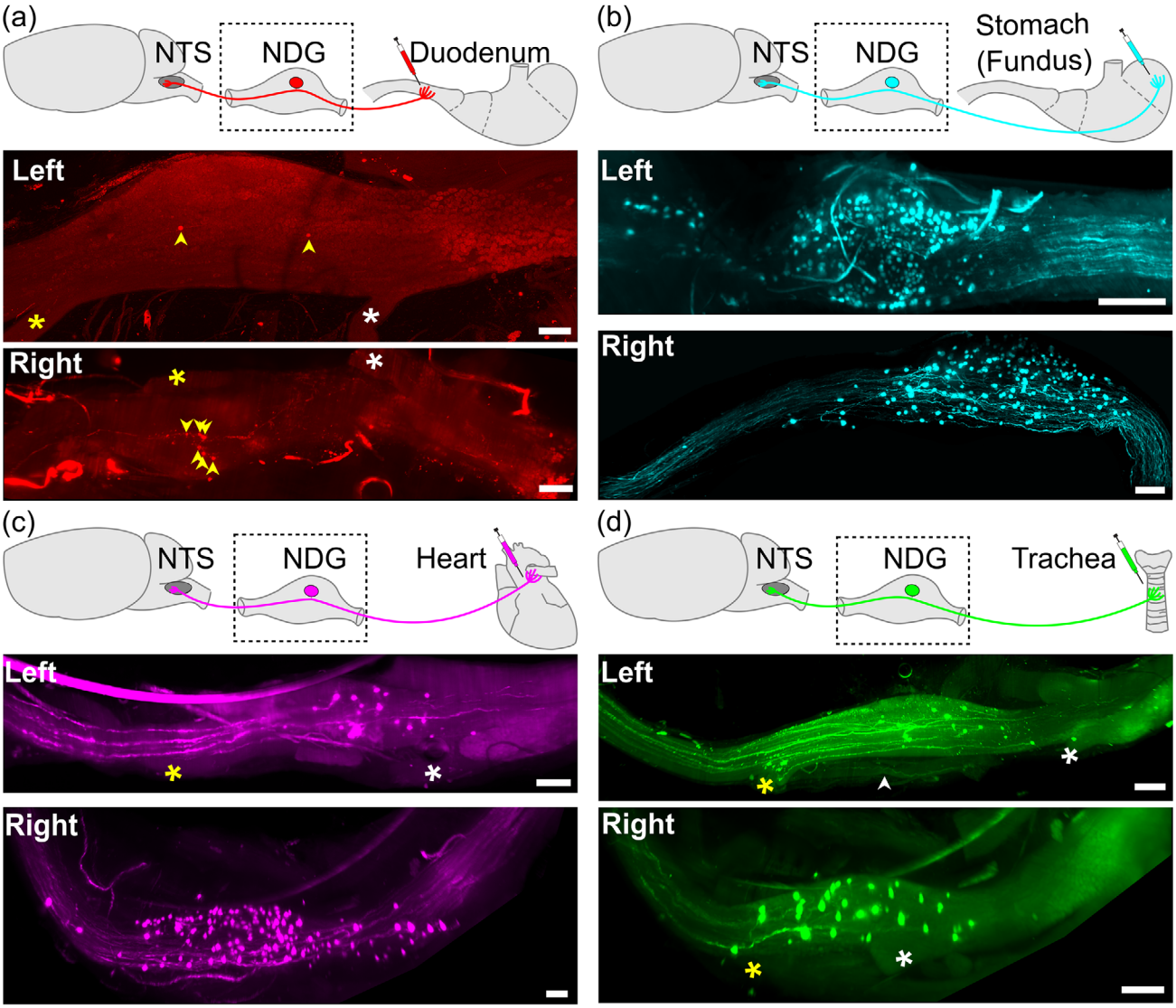

FIGURE 2 Organ-specific transduction of vagal viscerosensory neurons. The schematics illustrate the injection site for each panel. Photomicrographs of transduced nodose ganglion (NDG) neurons from cleared tissues following AAVrg injections in (a) duodenum; left: confocal, 258 μm *z*-stack; right: lightsheet, 804 μm *z*-stack; (b) stomach fundus; left: lightsheet, 844 μm *z*-stack; right: lightsheet, 1.1 mm *z*-stack; (c) heart; left: lightsheet, 748 μm *z*-stack; right: lightsheet, 1.1 mm *z*-stack and (d) trachea; left: lightsheet, 524 μm *z*-stack; right, lightsheet, 964 μm *z*-stack. Transduced NDG neurons are highlighted in (a) with yellow arrowheads. In the left NDG of (d), labeled axons traveling in the superior laryngeal nerve (*white arrowhead*) are shown. In most photomicrographs, the superior laryngeal nerve (*yellow asterisk*) and the glossopharyngeal nerve (*white asterisk*) are also visible. All images are maximum intensity projections. They are representative of $n = 20$. Scale bars are 100 μm except (c) right NDG scale bar = 200 μm

intermediate NTS, as the levels containing the AP (bregma −13.68 to −14.04 mm); and the caudal NTS as that caudal to the caudal border of the AP (bregma −14.04 to −16.00 mm). The stereotaxic coordinates are those derived from The Rat Brain in Stereotaxic Coordinates (Paxinos & Watson, 2004). To provide a qualitative index of the density of axonal labeling, we adopted the terminology of (Corbett et al., 2005) to divide densities into dense, sparse, or scattered categories.

In all peripheral organ injections, fluorescently labeled bundles of axons were observed to enter the brainstem at the rostral, dorsolateral surface, at bregma −11.00 mm, and then project horizontally to the dorsal midline to form the solitary tract (st). Dense fluorescent labeling was observed in the st throughout its entire length to bregma −16.00 mm. This observation of the trajectory of transduced afferent axons was consistent, albeit with lateralization reflecting the NDG labeling.

A consistent organization of axon labeling in the NTS was observed for each animal labeled from each peripheral organ. In all cases, the most robust labeling of axons was observed in the intermediate NTS. The overall pattern of labeling is shown as representative examples (Figure 3); in a graphical format (Figure 4); and as semi-quantitative data (Table 2). The overwhelming conclusion is that whilst there are differences in the density of labeling in different subnuclei

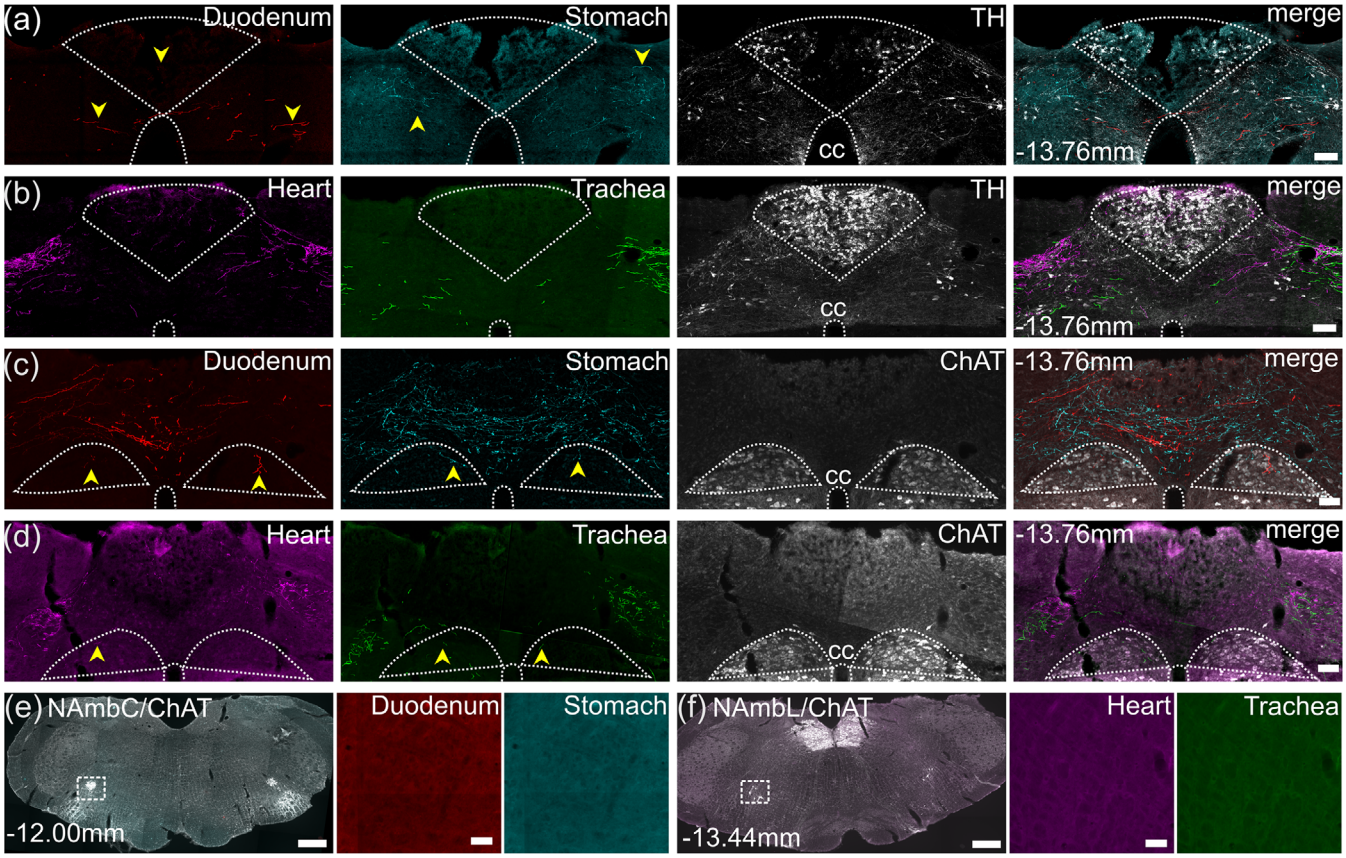

FIGURE 3 Transduction with AAVrg did not occur in parasympathetic efferent motor neurons or neurons of the area postrema. Epifluorescence images highlighting transduction in the area postrema (AP; a, b; *boundary shown with white dotted line;* −13.76 mm from bregma); dorsal motor nucleus of vagus (DMV; c, d; *boundary shown with white dotted line*; −13.76 mm from bregma); nucleus ambiguus (NAmb) at the level of the compact formation (NAmbC; e; −12.00 mm from bregma) and at the level of the loose formation (NAmbL; f; −13.44 mm from bregma). White neuronal profiles show immunoreactivity for tyrosine hydroxylase (TH; a, b) and choline acetyltransferase (ChAT; c–e). Higher magnification images of the left-hand side dotted boxed regions are shown adjacent to the lower magnification image in e and f. Transduction from injections in the duodenum are shown in red and stomach in cyan in a, c, and e. Transduction from injections in the heart are shown in magenta and trachea in green in b, d, and f. Yellow arrowheads indicate presence of vagal afferents axons. Note the absence of AAVrg transduced cells in AP, DMV, or NAmb. Scale bars are 100 μm (a–d), 200 μm (e and f, lower magnification) and 50 μm (e and f, higher magnification). Photomicrographs are from animals chosen as representative examples. *Abbreviations*: cc, central canal

corresponding to different peripheral targets, the visceral afferents show largely overlapping distributions throughout the NTS.

3.2 | Duodenum

AAVrg-CAG-tdTomato was injected into the serosal layer of the proximal, dorsal wall of duodenum (n = 3). At the injection site, axonal processes expressing tdTomato were observed in the muscle layer in processes with the morphology of intraganglionic laminar endings (Figure 1(a)) (Fox, Phillips, Martinson, Baronowsky, & Powley, 2000). As for all injected organs, we can be confident that many of the labeled processes at the injection site were derived from expression of fluorophore in the somata of transduced afferent neurons, which then diffused through the sensory neuron; however, we did also observe transduced intrinsic neurons. Processes from these cells would also contribute to the labeling within the peripheral organs, and, using our approach, we were not able to differentiate between the two sources.

Compared to injections in other organs, we observed a relatively low number of tdTomato expressing cell bodies in the NDG following duodenal injection (left: 4.7 ± 3.1 (0.07% of 6472 total Hu+ cells); right: 4.0 ± 4.4 (0.07% of 6092 total Hu+ cells); Table 1). The cell bodies were scattered across the ganglia (Figure 2(a)), with all animals showing dominance of labeling on one side. Interestingly, there was a difference in the lateral dominance between animals, and we conclude this is most likely due to variation in injection sites within the duodenum.

Reflecting the relatively small number of transduced neurons from the duodenal injections, vagal afferent axon labeling in the medulla oblongata was sparse, but the distribution widespread (Figures 3(a), 3(c), 4(a) and Table 2). It also showed lateral dominance correlating with the number and distribution of labeled cell bodies observed in NDG (Table 1 and Figure 4(a)). This is most clearly demonstrated by comparing Rat 2, with left dominance, and Rat 3, with right dominance (Figure 4(a)). Scattered axonal labeling was also observed in the DMV, particularly at more rostral levels, and the AP.

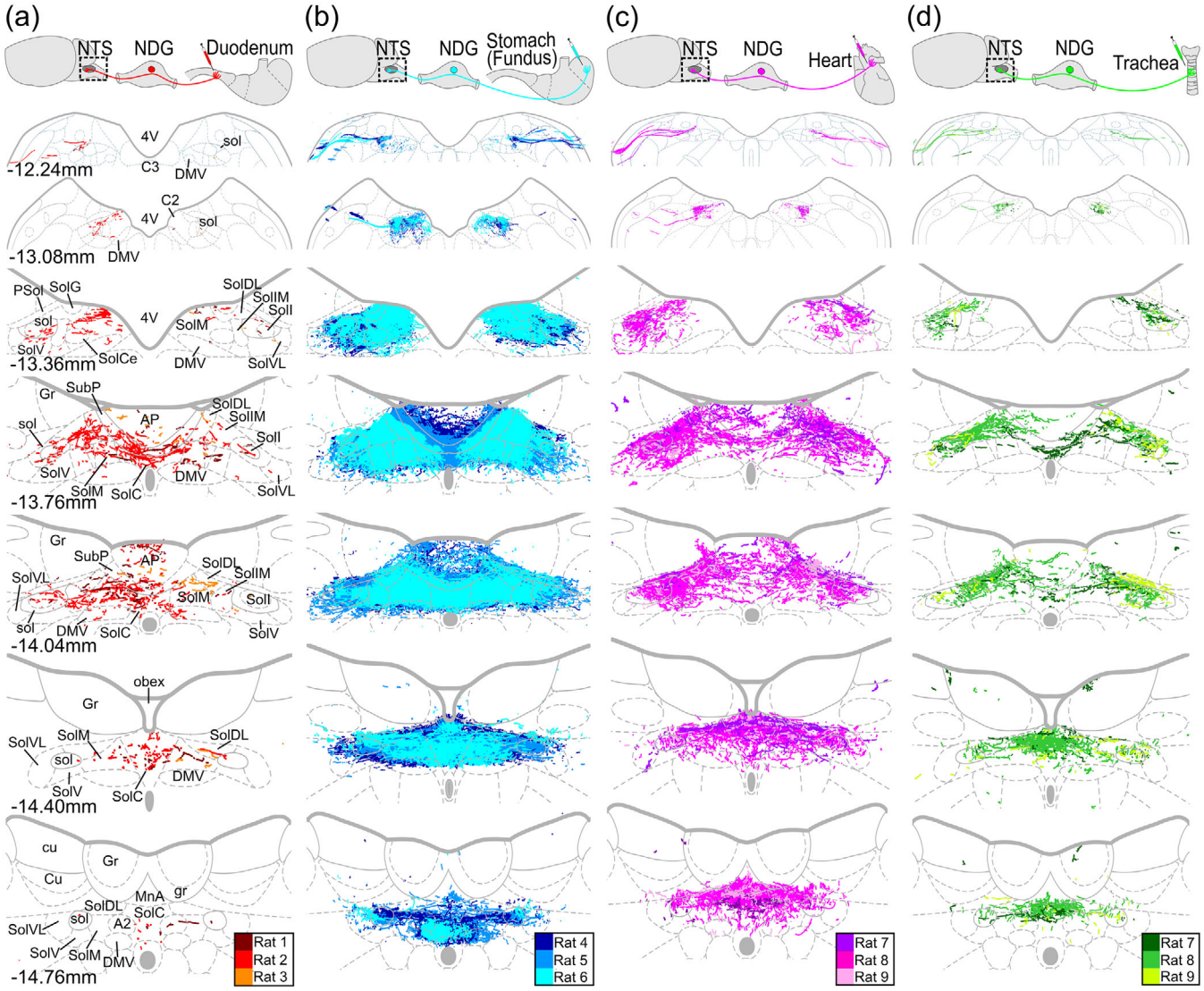

FIGURE 4 Maps of the distribution of transduced axons in the dorsal vagal complex following AAVrg injection in each peripheral organ. The schematics illustrate the injection site for each column (a) duodenum, (b) stomach, (c) heart, and (d) trachea. The maps show the distribution of transduced axons superimposed on coronal schematic images from rostral to caudal through the dorsal vagal complex. The size of each schematic map is adjusted to optimize space. The data show results from three animals per target organ injection. The key for each color and the corresponding rat number is shown at the bottom right of each column. The abbreviations for anatomical regions and the distance from bregma are shown in the left column but apply to all columns. *Abbreviations*: NDG, nodose ganglia; DMV, dorsal motor nucleus of the vagus; AP, area postrema; 4V, forth ventricle; C3, C3 adrenergic cell group; C2, C2 adrenergic cell group; A2, A2 noradrenergic cell group; MnA, median accessary nucleus; SubP, subpostrema nucleus; Gr, gracile nucleus; gr, gracile tract; Cu, cuneate nucleus; cu, cuneate tract; sol, solitary tract; PSol, parasolitary nucleus, NTS subnuclei – SolDL, dorsolateral part; SolC, commissural part; SolM, medial part; SolIM, intermediate part; SolV, ventral part; SolVL, ventrolateral part; SolI, interstitial part; SolCe, central part; SolG, gelatinous part

3.3 | Stomach

Injections of AAVrg-CAG-tdTomato were made into the serosal layer of the fundus ($n = 3$), and examination of tdTomato fluorescence, in cleared tissue, used to confirm the injection site. Fluorescently labeled axon processes traversed the serosal gastric wall and enveloped intrinsic neurons of the myenteric plexus, some of which were also transduced. The labeled afferent terminals had the morphology of intramuscular arrays and intraganglionic laminar endings (Figure 1(b)). Fluorophore expression occurred in cell bodies and axons in both the left and right NDG (Figure 2(b)). Similar number of cells were labeled in the left and right NDG in each animal, except in Rat 6 where there was a left predominance—this latter observation is likely due to variation in injection site (left: 218.7 ± 71.3 (3.4% of 6472 total Hu+ cells); right: 162.7 ± 64.3 (2.7% of 6092 total Hu+ cells); Table 1).

In addition to the distribution in the NTS (Figures 3(a), 3(c), 4(b) and Table 2), sparse axonal labeling occurred in the AP, DMV, subP, and the median accessory nucleus of the medulla (MnA). At caudal levels we also observed some labeled axons that appeared to enter the gracile nucleus (Gr).

TABLE 2 Comparative densities and distributions of organ-specific vagal afferent axons within the NTS. Duodenal, stomach, cardiac, and tracheal vagal axonal densities within the NTS were given dense (+++), sparse (++), and scattered (+) scores based on semi-quantification terminology used in Corbett et al. (2005). "–" indicates the absence of organ-specific vagal afferents within the NTS subnuclei. $n = 3$ per organ. *Abbreviations*: SolDL, dorsolateral part; SolC, commissural part; SolM, medial part; SolIM, intermediate part; SolV, ventral part; SolVL, ventrolateral part; SolI, interstitial part, SolCe, central part; SolG, gelatinous part; SubP, subpostrema nucleus

	Duodenum	Stomach	Heart	Trachea
Rostral NTS				
SolDL	+++	+++	++	++
SolM	+	++	+	–
SolG	+	+++	++	++
SolCe	+	+++	++	–
SolI	+	++	++	++
SolIM	–	++	+	+
SolV	–	+	+	+
SolVL	–	+	+	+
Intermediate NTS				
SolC	+++	+++	++	++
SolM	+++	+++	++	++
SolDL	+++	+++	+++	+++
SolIM	++	+++	++	++
SolI	++	++	+++	+++
subP	++	++	++	++
SolV	+	++	++	+
SolVL	+	++	++	+
Caudal NTS				
SolC	+++	+++	+++	+++
SolM	++	+++	++	++
SolDL	++	++	++	++
SolV	–	+	+	–
SolVL	–	+	+	–

3.4 | Heart

Injection of either AAVrg was made into the superficial dorsal atrial fat pad ($n = 3$) and the injection site confirmed by the presence of labeled nerve bundles, fine branches, and terminal endings in cleared tissue (Figure 1(c)). No labeling was observed in surrounding cardiac tissues including the aorta, atria, or ventricles.

Neurons were labeled throughout the rostro-caudal extent of the NDG, and in two rats there was no evidence of laterality in NDG labeling, whilst in one there was a right predominance (left: 50.0 ± 28.6 (0.8% of 6475 total Hu+ cells); right: 74.3 ± 42.2 (1.2% of 6092 total Hu+ cells); Table 1). The majority of labeled axons were observed in the vagal trunk near the NDG, but some were also seen in the superior laryngeal nerve (Figure 2(c) and Table 1). Rats 10 and 11 also showed three to four labeled cells in the JG on one side and terminals in the paratrigeminal nucleus (Pa5). There was no evidence of labeling in the petrosal ganglia (Figure 2(c)).

The distribution of labeled axons in the NTS is described (Figures 3 and 4 and Table 2). In contrast to labeling from the stomach and duodenum, no labeled axons were found in the DMV at the level of the rostral NTS. Scattered labeled axons were observed in the DMV at intermediate and caudal levels, as well as in the AP, Gr, MnA, and Cu.

In Rat 8, there were a few fluorescently labeled axons in the intermediate reticular nucleus (IRt), dorsal to the C1/A1 adrenergic cell group, and in a position ventral to the main vagal afferent fascicles, crossing the spinal trigeminal nucleus (Sp5I) and running along the parvicellular reticular nucleus (PCRt). It is possible that in this animal a small population of vagal efferent neurons was transduced, but we were unable to locate any transduced somata in either DMV or NAmb.

3.5 | Trachea

The AAVrg was injected into the epithelial layer of the posterior tracheal wall ($n = 3$) and the injection site confirmed by the presence of labeled terminals (Figure 1(d)). The fluorescently labeled NDG neurons were homogenously distributed along the rostral–caudal extent of the ganglia with a slight lateralization towards the right ganglia

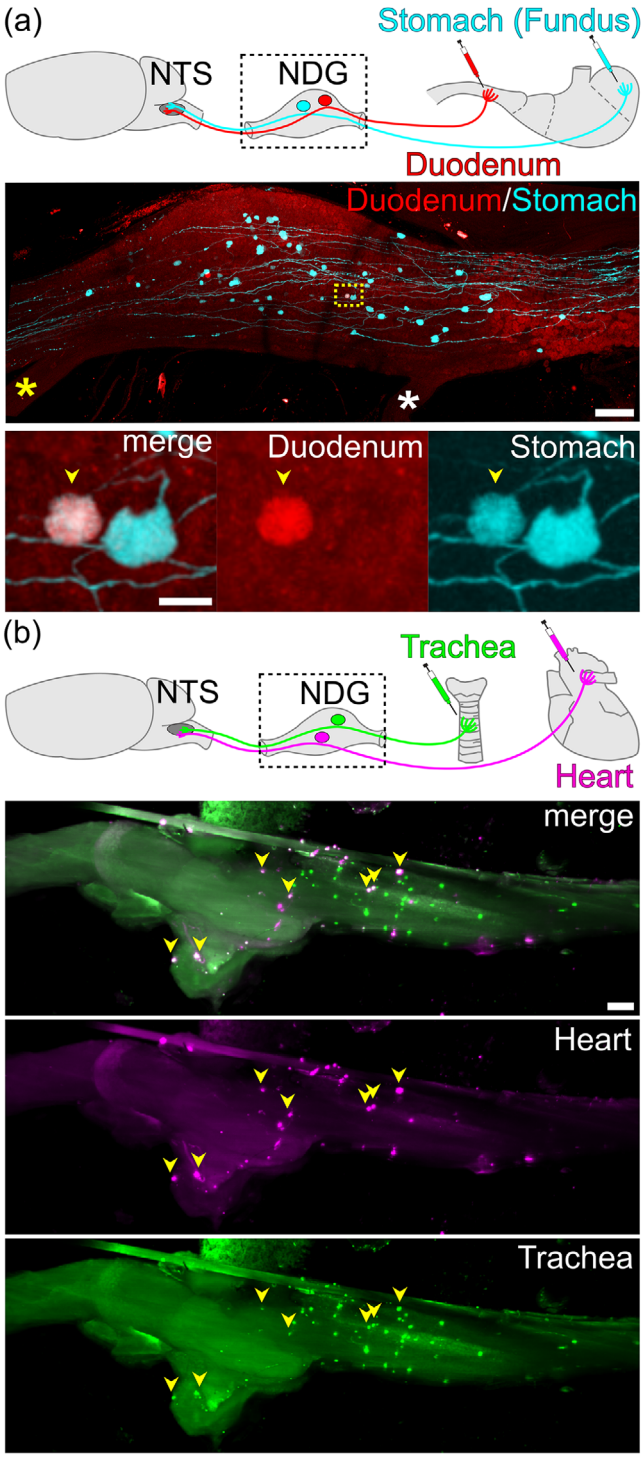

FIGURE 5 Distribution of transduced nodose ganglia (NDG) cell bodies in animals with dual AAVrg tracer injections. The schematics show the injection sites and color coding. (a) Photomicrograph of a confocal image (348 μm *z*-stack, scale bar = 100 μm) of a cleared NDG showing the distribution of neurons labeled from injections of different AAVrg in the stomach (cyan) and duodenum (red) in the same animal. The positions of the superior laryngeal nerve (yellow asterisk) and the glossopharyngeal nerve (white asterisk) are shown. The region of the dashed box is shown in higher power (48 μm *z*-stack, scale bar = 10 μm) and includes an example of a colabeled NDG cell (yellow arrowhead). (b) Photomicrograph of a Lightsheet image (1612 μm *z*-stack, scale bar = 200 μm) from a cleared NDG showing the distribution of transduced neurons following injection of different AAVrg in the heart (magenta) and trachea (green). Dual-labeled neurons are highlighted with the yellow arrowheads. All images are maximum intensity projections. Data are representative of injections in all animals

(Continues)

FIGURE 5 (Continued)

(Figure 2(d), left: 16 ± 9.2 (0.24% of 6472 total Hu+ cells); right: 28.3 ± 24.0 (0.5% of 6092 total Hu+ cells); Table 1). As with the heart afferents, the majority of labeled axons were observed to enter the ganglia via the vagal trunk, but some axons were also seen in the superior laryngeal nerve (Figure 2(d) and Table 1).

The distribution of labeled afferents is described (Figures 3(b), 3(d), 4(d), and Table 2). Particularly at intermediate and caudal levels, scattered axon labeling was observed in MnA (at the level of pyramidal decussations), AP, Gr, Cu, and DMV.

As for other rats, the vast majority of transduction was in vagal afferent axons. We did observe one axon in the ventral medulla emerging from the spinal trigeminal tract (sp5) and branching into intermediate spinal trigeminal nucleus (Sp5I), lateral to the C1 adrenergic cell group in Rat 7. In this rat, a few axons were also observed to enter slightly ventral to the main vagal fascicles, crossing the spinal trigeminal nucleus (Sp5I) and running along the parvicellular reticular nucleus (PCRt). It is possible these were vagal efferent axons, but transduced somata were not observed in DMV or NAmb. In Rat 9, a very small number of labeled fibers were seen in IRt dorsal to A1 adrenergic cell group. In Rat 18, which was not included in further analysis in this study due to very low levels of transduction, terminals were seen in the Pa5.

3.5.1 | Distribution of vagal afferent axons from two peripheral organs labeled in individual animals

The overwhelming impression of the results outlined above is that the distribution of fluorescently labeled axons in the NTS, following injections into different peripheral organs, is broadly similar. Any differences were related to variation in the density of innervation in particular subnuclei, likely reflecting the density of sensory innervation. No noteworthy examples of subnuclei selectively innervated from a specific organ were observed. To test this further, dual injections were made into like tissues, stomach fundus and duodenum or heart and trachea with AAVrg expressing either GFP or tdTomato.

3.6 | Stomach and duodenum

Within the NDG, cell bodies from each target were scattered across the ganglia without any distinct compartmentalization (Figure 5(a)). Stomach and duodenal afferents exhibited a similar distribution pattern within the NTS. Similar axonal labeling was observed from both targets as described above (Figures 6(a) and 6(b)). However, slight differences in density did become evident. Stomach afferents only were observed

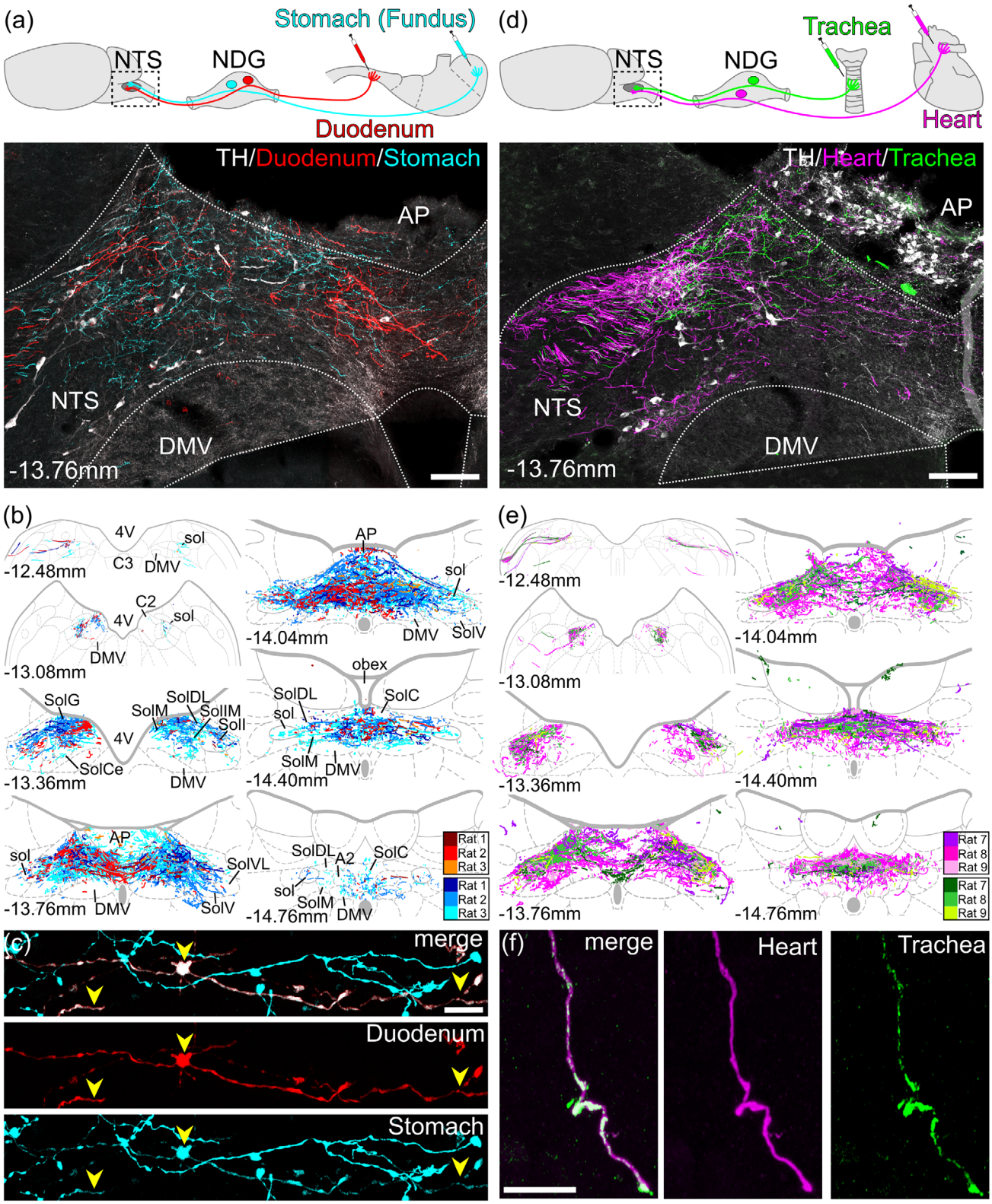

FIGURE 6 Distribution of vagal afferent axons in the nucleus of solitary tract (NTS) in animals with dual AAVrg tracer injections. The schematics show the injections sites and color coding. Representative confocal photomicrographs from individual animals showing the distribution of transduced afferent axons in the NTS (−13.76 mm from bregma) following microinjection of the same AAVrg expressing different fluorophores into the duodenum and stomach (a) or heart and trachea (d). Tyrosine hydroxylase (TH) immunoreactive neurons are shown in white. The scale bar = 100 μm. Panels (b) and (e) show data from all animals mapped onto coronal schematics of the medulla, arranged from rostral (top left) to caudal (bottom right) for each of the dual injections. The color code for each animal is shown. (c) A photomicrograph showing dual labeled afferent axons (*yellow arrowheads*) from dual AAVrg injections into proximal duodenum and stomach in the same animal (scale bar = 10 μm). Areas of overlap appear white in the merged image. (f) A photomicrograph showing a colabeled afferent axon from dual AAVrg injections into heart fat pads

(Continues)

FIGURE 6 (Continued)
and trachea (scale bar = 10 μm). All images are presented as maximum intensity projections and representative of all dual injected animals. *Abbreviations*: NDG, nodose ganglia; DMV, dorsal motor nucleus of the vagus; AP, area postrema; 4V, forth ventricle; C3, C3 adrenergic cell group; C2, C2 adrenergic cell group; A2, A2 noradrenergic cell group; MnA, median accessary nucleus; SubP, subpostrema nucleus; Gr, gracile nucleus; gr, gracile tract; Cu, cuneate nucleus; cu, cuneate tract; sol, solitary tract; PSol, parasolitary nucleus, NTS subnuclei – SolDL, dorsolateral part; SolC, commissural part; SolM, medial part; SolIM, intermediate part; SolV, ventral part; SolVL, ventrolateral part; SolI, interstitial part, SolCe, central part; SolG, gelatinous part

in the SolIM, SolV, and SolVL of the rostral NTS, and the MnO, DMV, SolVL, and Gr of the caudal NTS. Whilst this may indicate differences in overall distributions, it must be stated that afferent labeling from the duodenum was comparatively sparse and that this may account for the subtle differences in axon distribution.

In all of the dual labeled animals, we observed a small number of NDG neurons and NTS axons that were transduced by both AAVrg (Figures 5(a), 6(c), and Table 1). As the injection sites are anatomically isolated, this observation indicates rare NDG neurons project to both the stomach fundus and the duodenum.

3.7 | Heart and trachea

Within the NDG, cell bodies from each organ were distributed homogenously along the rostral–caudal extent of the ganglia without any distinct compartmentalization (Figure 5(b)). Within the NTS, subtle differences in the distribution pattern of afferents from these peripheral organs did become evident from this experimental approach (Figures 6(d) and 6(e)). In rostral NTS, only cardiac afferents branched into SolM, SolCe, SolV, and SolVL. In the intermediate NTS, the dense band of tracheal afferents was observed to extend bilaterally from the st to the SolI and SolDL and then diverge medially with sparse terminations in SolC, subP and AP. While the cardiac afferents were seen to follow a similar course, denser axonal labeling was observed medially in SolC, subP and AP. The projection of cardiac afferents into the DMV, SolVL, and SolV was obvious, whilst tracheal afferents were absent from these subnuclei. These differences were more prominent at the rostral level of AP. In the caudal NTS, while tracheal afferents formed a dense band confined to mainly the dorsal parts of SolC and SolM, the cardiac afferents were more broadly distributed and were denser in the A2 region, as well as the MnA and DMV. Cardiac afferent also extended into SolVL, SolV and Cu. A small number of colabeled NDG cells (Figure 5(b) and Table 1) and central terminals (Figure 6(f)) were observed in one of the three animals.

3.8 | Distribution of vagal afferent axons from a sparsely labeled peripheral organ in the NTS

The density of axonal labeling in the NTS, relative to the number of sensory afferent neurons transduced, suggested substantial divergence of innervation. To document this, we examined the central distribution of vagal afferent inputs from a sparsely labeled animal following AAVrg injection into the duodenum. In this animal (Rat 1), following rigorous examination, we could only detect two transduced vagal afferent neurons in the left NDG (Figures 7(a) and 7(b)), and one in the right NDG (Figure 7(c)). Despite this, we observed a distributed network of axons across the rostral–caudal levels of the dorsal vagal complex, particularly at intermediate and caudal levels of NTS and including the AP (Figure 7(d)). The left side of the NTS had greater density and branching of axons, with axon clusters predominantly in SolC, SolM, and SolDL and, to a lesser extent, SolI. Axons were either absent, or rare, at rostral and caudal levels. On the right side, axons were seen at intermediate levels predominantly in SolC and SolM, with scattered projections in Sol IM and SolI. At caudal levels scattered projections were observed in SolC and SolM and A2. At rostral levels scattered projections occurred in SolM, SolG, SolDL, and SolI. These observations demonstrate that individual vagal afferent neurons have a broad and divergent terminal field in the brainstem in both the rostral–caudal and medial–lateral axes.

3.9 | Close appositions of vagal afferents to second-order neurons in the dorsal vagal complex

Whilst the distributions of vagal afferent axons from different peripheral organs appeared to be very similar within the NTS, we reasoned that these might contact NTS neurons of different neurochemical phenotypes. Using high-resolution confocal microscopy, we examined the interaction between labeled afferents and NTS neurons immunoreactive for TH (Figure 8(a) and 8(e)), GLP-1 (Figures 8(b) and 8(f)), HSD2 (Figures 8(c) and 8(g)), and NK1R (Figure 8(d) and 8(h)), as well as DMV neurons immunoreactive for ChAT (Figure 9) and TH neurons in the AP (Figures 10 and 11(b)). Varicose vagal afferent axons from all target organs were observed to make close appositions to each of the neurochemically defined neuronal groups, with no apparent preference for a particular neurochemical phenotype with a subnucleus. We found evidence of a single afferent making close appositions, from sparse (Figure 8(g)) to dense (Figure 8(f)), onto single (Figure 9(b)), and/or multiple (Figure 9(a)) second-order neurons of a particular neurochemical type. We found evidence of multiple afferents from the same organ making close appositions with a single second-order neuron (Figure 8(a)). Most remarkably, in our dual viral injected animals, we found evidence of afferents from two different organs making close contacts with a single second-order neuron (Figures 11(a) and 11(b)).

Catecholaminergic neurons were examined in the NTS, between bregma −11.00 and −16.00 mm and the AP. The association of duodenal and stomach afferent with TH neurons was similar, with close appositions observed throughout the entire rostral–caudal length of the NTS and AP. The densest projections within the TH cell population occurred at the intermediate and caudal levels of NTS and AP,

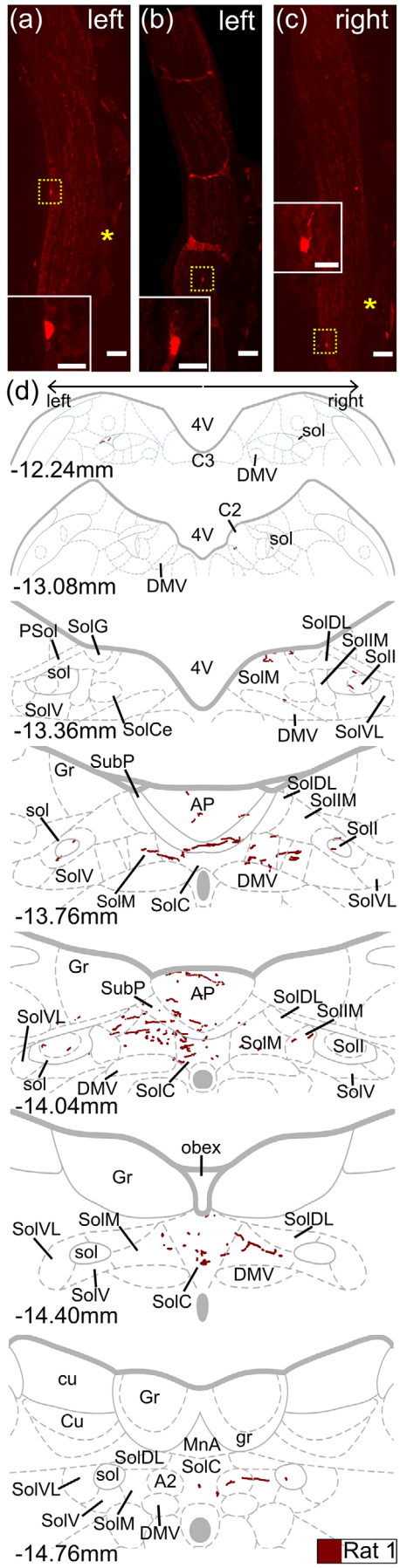

FIGURE 7 (Continued)

FIGURE 7 Distribution of transduced afferent axons in the nucleus of the solitary tract (NTS) following sparse labeling from the duodenum. All the neurons that could be identified following serial sectioning of the entire nodose ganglia bilaterally are shown in the photomicrographs (a–c). The position of the superior laryngeal nerve is highlighted with the yellow asterisk. Scale bar = 200 μm. The insets show a higher magnification of the labeled cells corresponding to the yellow dotted boxes. Scale bar = 50 μm. The distribution of all transduced duodenal afferent axons was mapped onto schematic maps of coronal brainstem sections (d). The position of each schematic section relative to bregma is shown. Data are representative of n = 3 with ≥2 transduced NDG cells per side. *Abbreviation*: DMV, dorsal motor nucleus of the vagus; AP, area postrema; 4V, forth ventricle; C3, C3 adrenergic cell group; C2, C2 adrenergic cell group; A2, A2 noradrenergic cell group; MnA, median accessary nucleus; SubP, subpostrema nucleus; Gr, gracile nucleus; gr, gracile tract; Cu, cuneate nucleus; cu, cuneate tract; sol, solitary tract; PSol, parasolitary nucleus, NTS subnuclei – SolDL, dorsolateral part; SolC, commissural part; SolM, medial part; SolIM, intermediate part; SolV, ventral part; SolVL, ventrolateral part; SolI, interstitial part, SolCe, central part; SolG, gelatinous part

respectively. Cardiac afferents displayed a consistently uniform distribution throughout the rostral–caudal extent of the TH cell population within the NTS and AP. However, the density of cardiac afferents among the TH cell population was less compared to that of gastric afferent terminals. Notably, the cardiac afferents had a more discrete correlation as these afferents were predominantly seen in the SolDM and SolDL. Tracheal afferents terminals followed a similar distribution pattern among the TH cells as the cardiac afferents but were considerably sparser at all levels of NTS and AP.

GLP-1 was used to label the preproglucagon (PPG) neurons that occur in the caudal NTS between -14.1 and -15.00 mm from bregma. Stomach and duodenal afferents were dense in the region of GLP-1 positive neurons throughout their rostral–caudal extent in the NTS, making many close appositions. Most duodenal, but only rare stomach, afferents were GLP-1 positive, including some duodenal afferents with close appositions to PPG neurons (Figure 11(c)). Cardiac and tracheal afferents were also observed to project to the PPG cell population, though less dense when compared to the gastric and duodenal afferents. The majority of tracheal afferents were GLP-1 positive (Figure 11(d)), including some with close appositions to PPG neurons, whilst no cardiac afferents were GLP-1 positive. To our knowledge, expression of PPG has not been described previously in vagal afferents, including in RNAseq analysis of NDG neurons in the mouse (Bai et al., 2019).

Immunoreactivity for HSD2 was used to characterize the aldosterone and salt-sensitive neuronal subpopulation in the NTS (Geerling et al., 2006). These neurons were located between −13.60 and −15.00 mm from bregma, with the densest population rostrally lining fourth ventricle. Both stomach and duodenal afferent were seen among the HSD2 neurons, particularly in the caudal and intermediate NTS cluster. Heart and tracheal afferent terminals were also present among the HSD2 cells but were considerably sparser compared to the

(Continues)

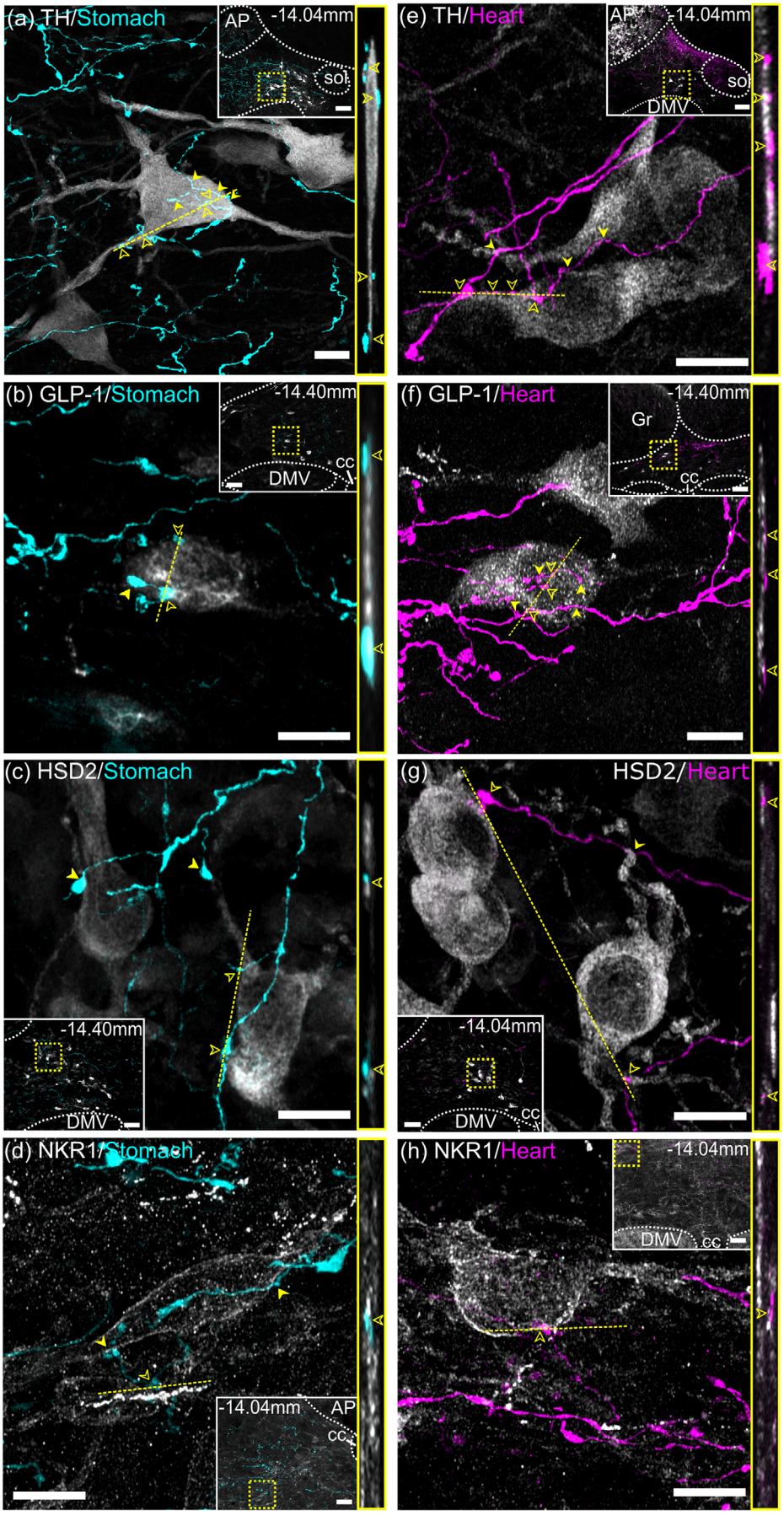

(Continues)

FIGURE 8 (Continued)

FIGURE 8 Close appositions between vagal afferent axons and nucleus of the solitary tract (NTS) neurons. Confocal photomicrographs showing transduced axons following injection of AAVrg into the stomach (cyan; a–d) and heart (magenta; e–h). NTS neurons of different neurochemical phenotype are shown in the rows with white showing immunoreactivity for tyrosine hydroxylase (a, e); glucagon-like peptide 1 (b, f); 11ß-hydroxy-steroid dehydrogenase type 2 (c, g); or neurokinin receptor 1 (d, h). Close appositions are highlighted with yellow arrowheads. The scale bar represents 10 μm for all sections. The insets in each image show a lower magnification epifluorescence photomicrograph of the NTS region with the yellow dotted box corresponding to the higher magnification main image. The scale bars represent 100 μm. The panels to the right side of each image show a "side view" of close appositions highlighted with open yellow arrowheads in the main image. The side view is a single plane generated by reslicing *z*-stack image along the depicted yellow dotted line. All images are presented as maximum intensity projections. *Abbreviations*: AP, area postrema; DMV, dorsal motor nucleus of the vagus; cc, central canal; sol, solitary tract; Gr, gracile nucleus; 4V, forth ventricle

afferents from the gastrointestinal organs. The cardiac and tracheal afferents were also homogenously spread across the rostral–caudal extent of the HSD2 cell cluster.

The NK1R neurons were located in the NTS and DMV between -11.00 to -16.00mm from bregma with the densest population at intermediate and rostral levels. Gastric and duodenal afferent terminals were observed among the NK1R positive neurons with the densest projections seen at the intermediate NTS levels. Cardiac and tracheal afferents were also observed among NK1R positive neurons albeit to a lesser extent. Interestingly, all afferent subtypes, except cardiac, also showed sparse distribution among NK1R positive DMV neurons.

The overall density of afferent projections to cholinergic DMV neurons was sparse from all peripheral organs but with distinct differences in rostral–caudal distributions. The most prominent afferent distribution in DMV was seen from the stomach and to a lesser degree from the duodenum. Most stomach projections to the DMV were at the level of caudal and intermediate NTS. Few associations were observed at the level of the rostral NTS. Sparse duodenal afferents were mostly present in DMV at the intermediate levels of NTS and scattered distributions at rostral NTS levels. Duodenal afferents were not observed in the caudal DMV. Cardiac afferent projections to the DMV were sporadic, occurring at caudal and intermediate levels of NTS and absent from rostral levels. Tracheal afferents in DMV were only seen at caudal levels of NTS and were absent at intermediate and rostral levels of NTS. Further supporting the observation that in these experiments AAVrg exhibited no tropism for parasympathetic preganglionic efferent neurons, ChAT immunoreactivity was not present in any of the retrogradely labeled afferents.

3.10 | Putative sensory afferent synapses—distribution and counts

The overlapping distributions of afferent axons within the NTS, that were transduced from distinctly different peripheral targets, led us to question how much of the labeling within a subnucleus represented synapses within that subnucleus versus axons of passage heading to their synapse. We observed close appositions between transduced afferents and neurochemically defined NTS neurons throughout the extent of the NTS, indicative of widespread synaptic interaction. To further test this observation, we mapped the location of synaptic terminals from stomach afferents within the dorsal vagal complex. Using the same surgical injection approach as for the AAVrg mapping studies, stomach vagal sensory afferents from the fundus were transduced with AAV9-hSyn1-Cre. Bilateral injections of AAVDJ8-hSyn-FLEX-mGFP-2A-Synaptophysin-mRuby into the NDG enabled expression of membrane bound GFP (mGFP), that fills both soma and axons, and synaptophysin fused to mRuby (Syp-mRuby), to label presynaptic terminals, in Cre-expressing, stomach projecting NDG neurons (Figure 12(a)). The distribution of labeled stomach afferents was similar to that described above. The Syp-mRuby, which presented as puncta within the mGFP labeled axons, was considered to mark putative synapses. These, too, were distributed across their entire rostral–caudal distribution within the dorsal vagal complex (Figure 12(b)–12(f)). In support of the conclusion that the Syp-mRuby labeled biologically significant synapses rather than just having a random distribution, we observed that the synaptic density was variable and not correlated with the density of afferents present within a subregion. In the rostral NTS, most Syp-mRuby was observed in SolI, SolDL and SolG with sparser distributions in SolL, SolVL, solIM, and dorsal SolM (Figure 12(c)). The densest distribution of Syp-mRuby occurred within the intermediate NTS, most notably in SolI (Figure 12(e)). Within the intermediate NTS Syp-mRuby was also observed in the SolC, SolM, SolIM, SolDL, SolV as well as in the AP and DMV (Figures 12(d) and 12(e)). In the caudal NTS, dense Syp-mRuby occurred within the SolM, SolDL, and SolC, with a sparser distribution in SolVL, SolV, A2, and in the DMV (Figure 12(f)). High-resolution confocal imaging revealed that the majority of the Syp-mRuby immunolabeling was in bouton-like structures (Figure 12(g)). However, we also noted some labeling in axons, including those in the st and in the rostral vagal fascicles coursing between the dorsolateral surface of the medulla and the st (Figure 12(b)). In these regions it is unlikely the presence of Syp-mRuby indicates the presence of synapses, and this brings into question the validity of using the presence of Syp-mRuby to identify presynaptic labeling. We reasoned that whilst Syp-mRuby labeling might provide a gross distribution pattern of putative synaptic sites, in our observations the data would be an overestimation of the presence of true synapses.

To characterize putative synapses in the NTS, stomach afferents were transduced with AAVrg expressing tdTomato or GFP and the pre- and postsynaptic markers, synapsin-1 and PSD95 respectively, were visualized using immunohistochemistry (Figures 13(a) and 13(b)). Using high-resolution confocal microscopy, a putative synapse was

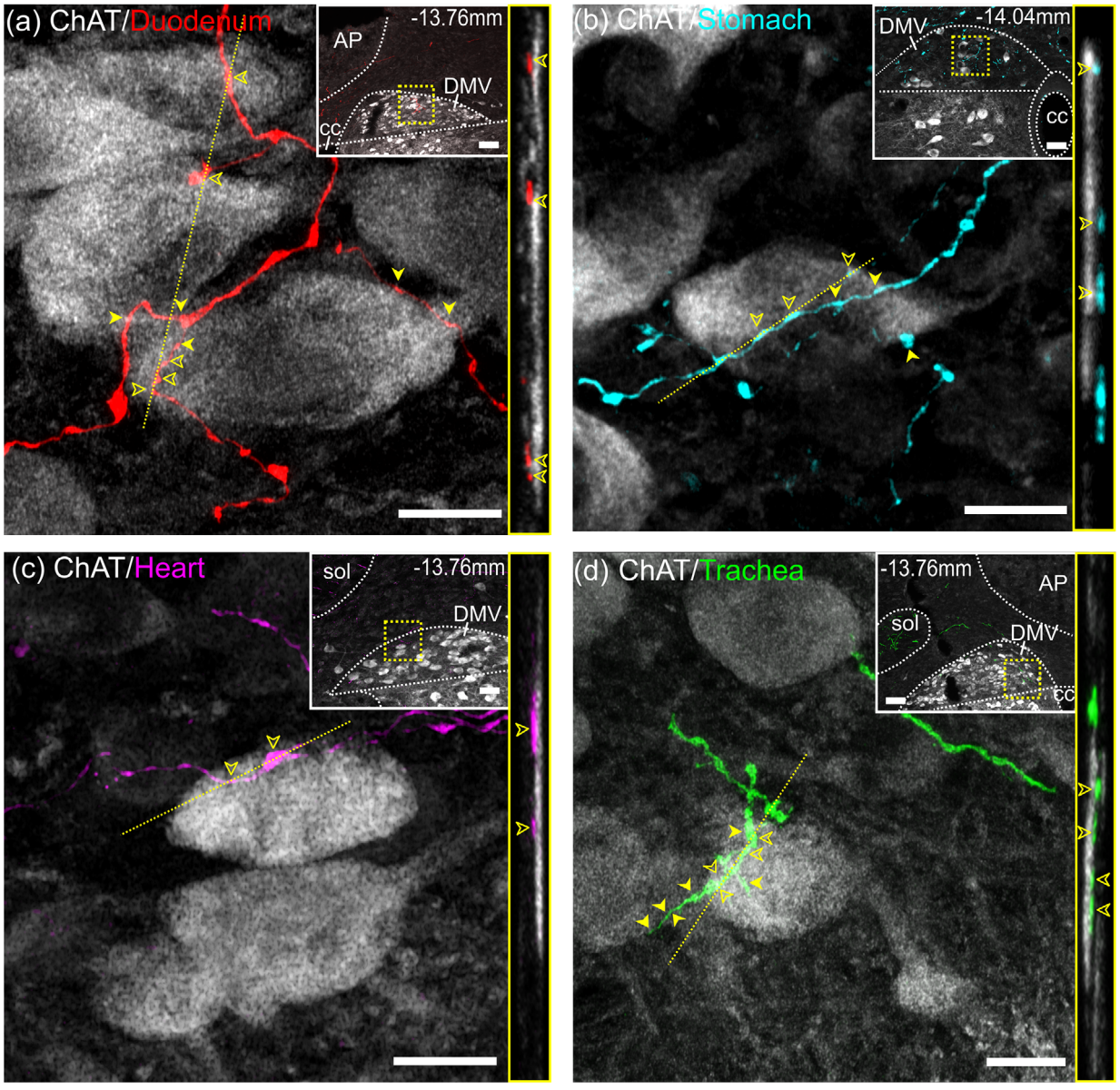

FIGURE 9 Close appositions between transduced afferent axons and dorsal motor nucleus of vagus (DMV) neurons. Confocal photomicrographs showing transduced vagal afferent axons following injection of AAVrg into (a) duodenum; (b) stomach; (c) heart; and (d) trachea. The scale bar in the main images represents 10 μm. The white images show immunoreactivity for ChAT in DMV parasympathetic preganglionic neurons. The insets in each image show a lower magnification epifluorescence photomicrograph of the dorsal vagal complex, with the dotted yellow box corresponding to the main higher magnification images. The scale bar represents 100 μm. The yellow arrowheads highlight close appositions. The panels to the right side of each image show a "side view" of close appositions, depicted by open yellow arrowheads in the main image, in a single plane after reslicing *z*-stack image along the depicted yellow dotted line. All images are presented as maximum intensity projections. *Abbreviations*: AP, area postrema; cc, central canal; sol, solitary tract

defined as an overlapping pair of pre- and postsynaptic "puncta" near the surface of an afferent axon (Figures 13(a)–13(d)). Counts of putative synapses were performed on a 50 μm length of each afferent fiber, using automated methods to avoid operator bias (n = 3). The average putative synapse numbers were similar between subnuclei at the same NTS level, and also in subnuclei across different NTS levels (Figures 13(f) and 13(g)). Average putative synapse counts along the same afferent fiber were also similar between lateral segments, close to the st, and medial segments (Figures 13(f) and 13(g)). Using this approach, we still observed putative synapses in the rostral vagal fascicles, but these were much lower in number than those in the NTS subnuclei, suggesting that our putative synapse detection and counting protocol was selective for true putative synapses, and that fascicular labeling could be considered background. From these observations we conclude that vagal afferents make widespread putative synapses across multiple NTS subnuclei and that the distribution of putative synapses is likely reflected in the distribution of fluorescently labeled afferents of transduced neurons.

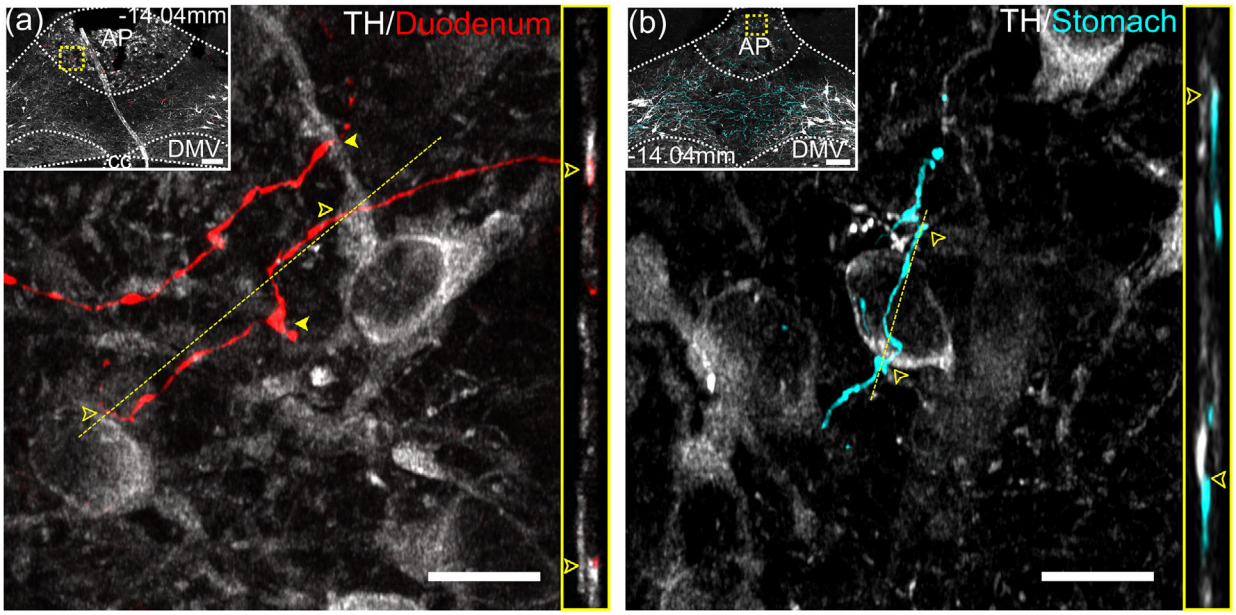

FIGURE 10 Close appositions between transduced afferent axons and area postrema (AP) neurons. Confocal photomicrographs showing transduced vagal afferent axons in the AP following injection of AAVrg into (a) duodenum; and (b) stomach. Immunoreactivity for tyrosine hydroxylase (TH) is shown in white. Close appositions are highlighted with yellow arrowheads. The scale bar in the main images represents 10 μm. The insets in each image show a lower magnification epifluorescence photomicrograph of the NTS region with the yellow dotted box corresponding to the higher magnification image. The position relative to bregma is shown and the scale bars represent 100 μm. The panels to the right side of each image shows a "side view" of close appositions, highlighted with open yellow arrowheads in the main image, in a single plane after reslicing the *z*-stack image along the depicted yellow dotted line. All images are presented as maximum intensity projections. *Abbreviations*: AP, area postrema; cc, central canal; DMV, dorsal motor nucleus of the vagus

To further refine our paradigm and reduce counting of false pre- and postsynaptic pairs due to random associations (Sauerbeck et al., 2020), synapse quantification was performed in the presence of pan-neuronal marker, HU (Figure 13(e)), which stains the soma. A putative synapse was redefined as an overlapping pair of presynaptic "puncta," in close proximity to the surface of an afferent axons, and a postsynaptic "punctum" near the somal surface of a second-order neuron (Figure 13(e)). The synapse counts using this "somal biased" method, shown in pink on Figure 13(a) ($n = 1$), were considerably less than the previous synapse counts within the same NTS subnuclei. The putative synapses were mainly detected in the intermediate levels of NTS within SolC, SolM, SolIM, and SolDL. No putative synapses were detected in the lateral segments of the afferent axon compared to medial segment suggesting that as axons exit the st, they are more likely to cross to medial parts of the NTS to make synaptic contacts. Of course, we cannot rule out that the axons make synapses with segments of the neuron that does not express detectable levels of Hu. Overall, we can conclude from our observations that (1) single vagal sensory afferent axons make numerous putative synapses within a NTS subnuclei and (2) that these axons show substantial divergence, targeting multiple NTS subnuclei.

4 | DISCUSSION

Injection of AAVrg into the stomach fundus, duodenum, cardiac atria fat pads, or trachea induced fluorophore expression in vagal sensory neurons, and enabled examination of their peripheral projections, somata, and central projections to the NTS. Vagal afferent sensory endings within the peripheral organs, visualized by the presence of fluorophore that diffused from the somata of transduced NDG neurons, showed morphological characteristics as described previously (Baluk & Gabella, 1991; Berthoud & Powley, 1992; Fox et al., 2000; Powley et al., 2019; Prescott et al., 2020). In agreement with previous publications (Altschuler et al., 1989; Andresen & Paton, 2011; Y. Bai et al., 2019; Muller et al., 2020; Williams et al., 2016; Zhao et al., 2022), we observed a homogenous distribution of somata within the NDG, with no apparent topographical organization relating to peripheral targets. By utilizing the same viral vectors and analytical methods to examine four different peripheral targets, as well as dual labeling from specific targets in some animals, we generated comprehensive maps that support an overwhelming conclusion that vagal sensory neurons innervating each organ terminate in multiple NTS subnuclei, with dramatic overlapping distributions and little evidence of viscerotopic organization. In one sparsely labeled animal, with just three NDG neurons transduced following a duodenal injection, we observed widespread axonal divergence, with the axonal processes observed throughout the rostrocaudal axis of the NTS and in multiple subnuclei. Examination of specific post and presynaptic protein distribution indicated that vagal afferents make multiple putative synapses as they course through the NTS. In addition to an apparent lack of anatomic and somatotopic organization of inputs, we observed close appositions between transduced vagal afferents from different organs and a wide range of

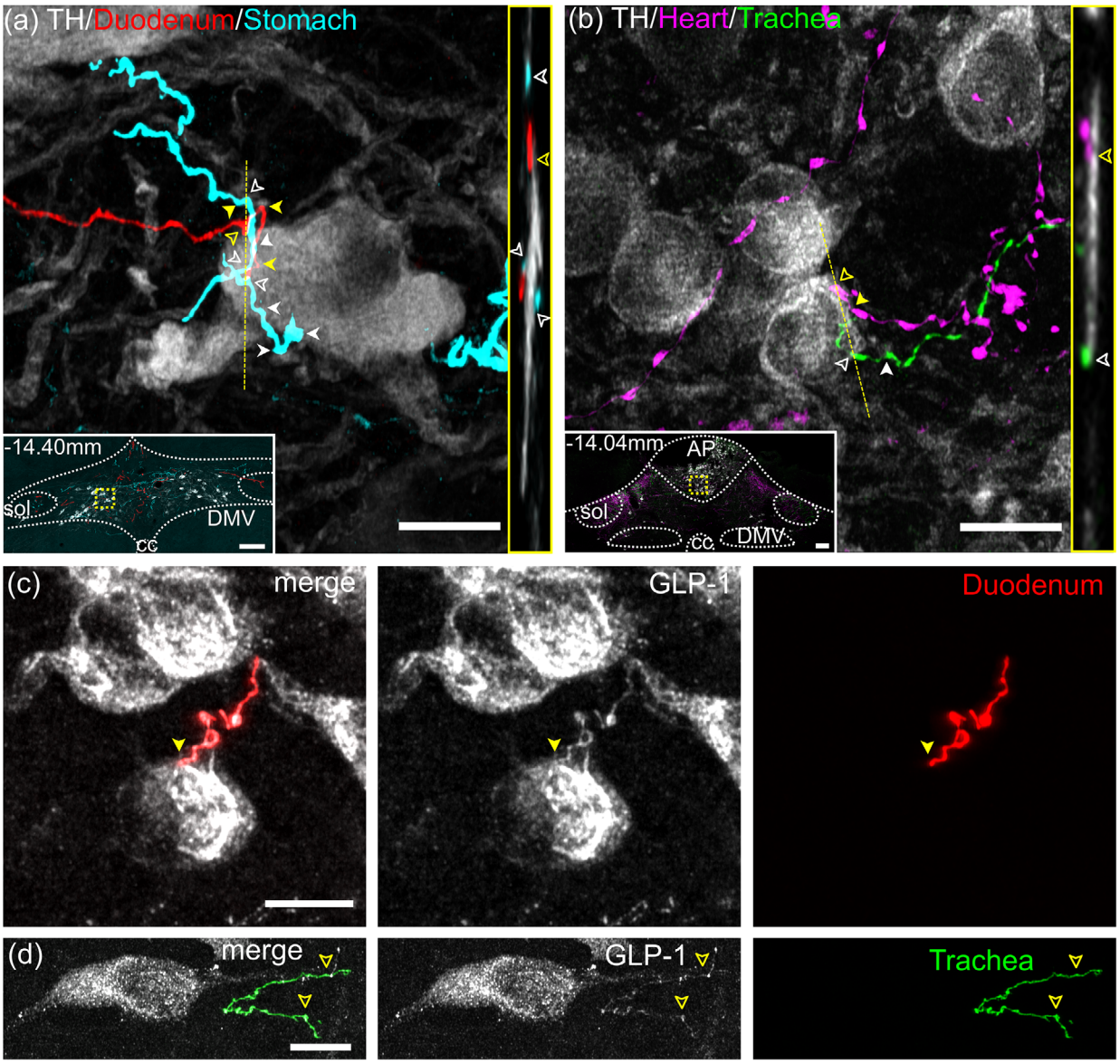

FIGURE 11 Close appositions between afferent axon transduced from different organs and individual nucleus of the solitary tract (NTS) neurons. Duodenal and tracheal afferent axons express GLP-1. In one rat (a) afferent neurons were transduced from the duodenum (red) and stomach (cyan), whilst in another (b) afferents were transduced from the heart (magenta) and trachea (green). The confocal photomicrograph showing close appositions, highlighted by arrowheads, between transduced axons and tyrosine hydroxylase (TH) immunoreactive NTS neurons, shown in white. The scale bar represents 10 μm. The insets in each image show a lower magnification epifluorescence photomicrograph of the NTS region, including the position relative to bregma, with the yellow dotted box corresponding to the higher magnification image. The inset scale bar represents 100 μm. The panels to the right side of each image shows a "side view" of close appositions, highlighted by the open arrowheads in the main image, in a single plane after reslicing *z*-stack image along the depicted yellow dotted line. (c) Confocal photomicrograph of a duodenal afferent axon (red) expressing GLP-1 in close apposition, highlighted by arrowhead, to GLP-1 expressing NTS neuron (white). (d) Confocal photomicrograph of a tracheal afferent axons (green) expressing GLP-1 (highlighted by open arrowheads). Scale bars represent 10 μm. All images are presented as maximum intensity projections. *Abbreviations*: AP, area postrema; cc, central canal; DMV, dorsal motor nucleus of the vagus; sol, solitary tract

neurochemically diverse cell populations in the dorsal vagal complex-again with little evidence of preferential distribution amongst cell types. Gastric, duodenal, cardiac, and tracheal afferents were found in close apposition to TH, GLP-1, HSD2, and NK1R cells in the NTS, TH cells in AP, and ChAT cells in DMV. Furthermore, vagal afferents from different organs were observed to contact the same second-order neuron in NTS and AP. In agreement with previous literature, we conclude that vagal afferent inputs to NTS neurons lack a readily apparent viscerotopic organization, with each afferent showing substantial divergent input throughout the NTS.

The widespread and overlapping distribution of transduced axons throughout the NTS following peripheral target injections led us to

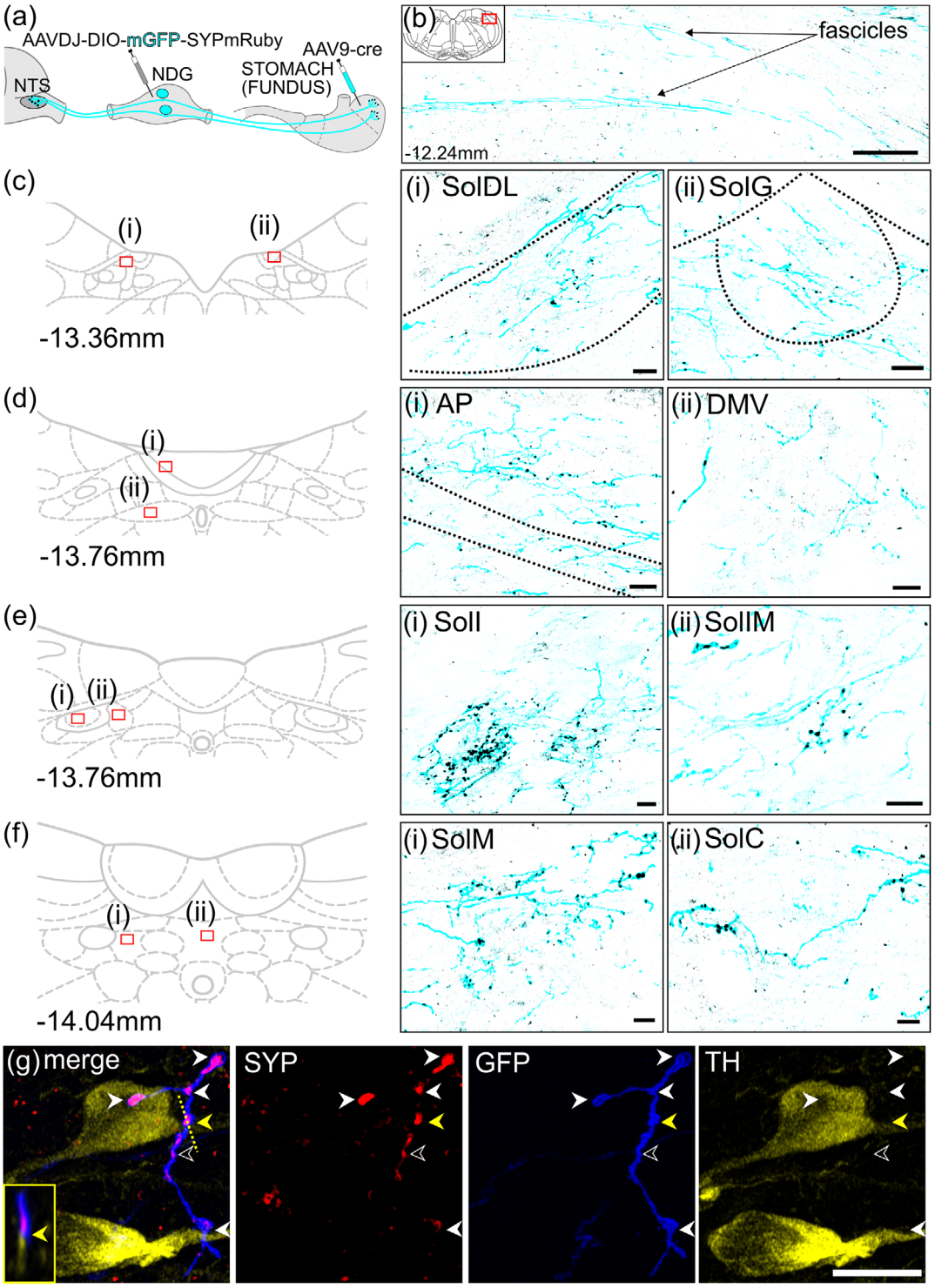

FIGURE 12 Putative vagal afferent synapses in the dorsal vagal complex. A schematic showing the protocol, in which AAV9-Cre is injected into the stomach fundus and AAV delivering Cre-dependent expression of membrane-bound GFP (mGFP) and synaptophysin (SYP)-mRuby is injected into the NDG (a). Confocal photomicrographs of coronal brainstem section showing the distribution of stomach-specific afferent axons (*cyan*) with putative presynaptic terminal sites labeled with SYP-mRuby (*black*) in the rostral vagal fascicles (b) and select NTS subregions is shown (c–f). For each subregion, a schematic coronal brainstem section is shown with position of the photomicrographs depicted as a red box (i, ii). The position of each image relative to bregma is shown. The scale bar represents 100 μm (b) and 20 μm (c–f). (g) High-resolution confocal images of the same section showing a stomach-specific afferent axon, labeled with GFP, but shown in blue; synaptic boutons labeled with SYP-mRuby, shown in red, and immunoreactivity for tyrosine hydroxylase (TH) in yellow. The images are shown in individual colors and also as a merged image. SYN-mRuby positive boutons that are not in close apposition to the TH immunoreactive neuron are highlighted with white arrowheads.

(Continues)

FIGURE 12 (Continued)
SYN-mRuby expression in an axon is shown with white open arrowheads. A bouton in close apposition to a TH immunoreactive process is highlighted with a yellow arrowhead. The inset shows a "side view" of the close apposition highlighted with the *yellow arrowhead* in single plane after reslicing z-stack image along the depicted yellow dotted line. The scale bar represents 10 μm. All images are presented as maximum intensity projections. *Abbreviation*: AP, area postrema; DMV, dorsal motor nucleus of the vagus; NTS subnuclei - SolDL, dorsolateral part; SolC, commissural part; SolM, medial part; SolIM, intermediate part; SolI, interstitial part; SolG, gelatinous part

question whether the use of fluorophore expression to label axonal processes actually provides an indication of synaptic input at multiple levels of the nucleus or whether it might just indicate a tortuous path followed by the axon to reach its site of synapse. Our high-resolution light microscopic data, examining colocalization of transduced afferents and putative pre- and postsynaptic markers, indicate that vagal afferents make multiple putative synaptic connections in many different subnuclei as they course through the NTS. Using a viral approach to label a presynaptic marker in vagal afferents from the stomach, we generated a distribution map of putative synapses that showed putative synaptic inputs across the dorsal vagal complex. This was further supported by automated synapse quantification analysis, which showed that the putative vagal afferent synapses are uniformly distributed across NTS subnuclei, thus highlighting the divergence of these afferent inputs centrally. Previous physiological studies of respiratory-related afferent neurons, combined with anatomical reconstruction, also indicate that single afferents had hundreds of synaptic boutons distributed throughout the rostrocaudal plane of the NTS and in multiple subnuclei (Kalia & Richter, 1988). The evidence indicates that substantial divergence of vagal afferent input with no specific population of second-order neurons, or NTS subregion, being exclusively innervated by afferents from a specific organ. An afferent begin to branch and synapse early upon exit from the solitary tract and makes multiple contacts with second-order NTS neurons, sometimes of different neurochemical phenotype. The implication of this is that specific visceral sensory modalities are widely distributed spatially to different populations of second-order NTS neurons.

4.1 | Organization of sensory input to the NTS

Our observations might suggest that sensory modality rather than somatotopy is the principal organizing factor within the NTS. Each organ is innervated by a diverse range of peripheral sensory receptors (Paintal, 1973), that have specific spatial distributions, neurochemical codes and electrophysiological properties (Berthoud & Neuhuber, 2000; Mazzone et al., 2020; Powley et al., 2019; Wang et al., 2020). However, even on this basis, whilst some sensory modalities are shown to have preferential input to a specific subnucleus, for example respiratory slow adapting receptor afferents to SolC/SolM and rapidly adapting receptor afferents to SolVL (Kalia & Richter, 1985, 1988; Kubin, Alheid, Zuperku, & McCrimmon, 2006), considerable input to other subnuclei occurs. The question remains as to how this preferential modality-based organization might translate to the organization of second-order neurons? When measured in slices in vitro, ~30% of second-order neurons receive multiple inputs (McDougall, Peters, & Andresen, 2009). Functional studies in vivo support this but provide evidence of specific modality input to NTS neurons. Putative second-order NTS neurons receive convergent input from pulmonary C fiber, cardiac receptor and peripheral chemoreceptor receptors (Mifflin, 1996; Paton, 1998), but do not respond to information related to cardiovascular pressure (Paton, 1998). Similarly, NTS neurons receiving afferent information from the subdiaphragmatic vagus do not respond to arterial baroreceptor or chemoreceptor stimulation (Paton, Li, Deuchars, & Kasparov, 2000). Activation of different afferent branches appears to show convergence onto ~ 15% of NTS neurons (Bonham & Hasser, 1993; Donoghue, Felder, Gilbey, Jordan, & Spyer, 1985; Mifflin, 1996; Ootani, Umezaki, Shin, & Murata, 1995). Unfortunately, we do not have a clear understanding of how these, at least partially modality specific NTS neurons, are organized anatomically. Some studies do show segregation of second-order NTS neurons based on the expression of transient receptor potential V1 receptors in the afferent neuron (Peters, McDougall, Fawley, & Andresen, 2011), or the target of the second-order NTS axon projections (Bailey et al., 2006; McDougall, Guo, & Andresen, 2017). Using our approaches, we were not able to differentiate input from a specific organ into different modalities, despite examining input onto several different neurochemical classes of NTS neurons. Indeed, we observed inputs from different organs onto the same neurochemically identified NTS neurons. It is possible that novel activity-based methods, such as Fos-TRAP might shed further light on this (J. Chen et al., 2020). Many second-order NTS neurons appear to be in a position to receive the same sensory input as it is distributed through the NTS by individual vagal sensory neurons. This anatomical arrangement likely underlies the integration needed to coordinate autonomic reflexes and influence neuroendocrine and emotional valence at the earliest stages of visceral sensory processing. Clearly, the organization of the NTS is complex, even compared with regions such as the spinal dorsal horn, which have similar functions in receiving, modulating and integrating peripheral sensory information (Janig & Habler, 2002), and will require an understanding of target and modality properties of the afferent combined with neurochemical and projection properties of the second-order NTS neuron.

The evidence provided in this study suggesting substantial, divergent, and overlapping sensory input from different organs is not congruent with some previous reports. We suggest this can be due to differences in the labeling approaches that require careful interpretation. Conventional dyes and tracers have the following characteristics: they tend to be nonspecific in that they label both vagal afferent and efferent neurons (Altschuler et al., 1989; Shapiro & Miselis, 1985); they exhibit variable diffusion in the target tissue (Hunter & Undem, 1999); they exhibit biased uptake, for example, the cholera toxin b subunit tracer preferentially labels myelinated afferents (Hermes, Colbert, & Aicher, 2014; Herrity, Rau, Petruska, Stirling, & Hubscher, 2014); and they are inefficiently transported along highly branched axons, for

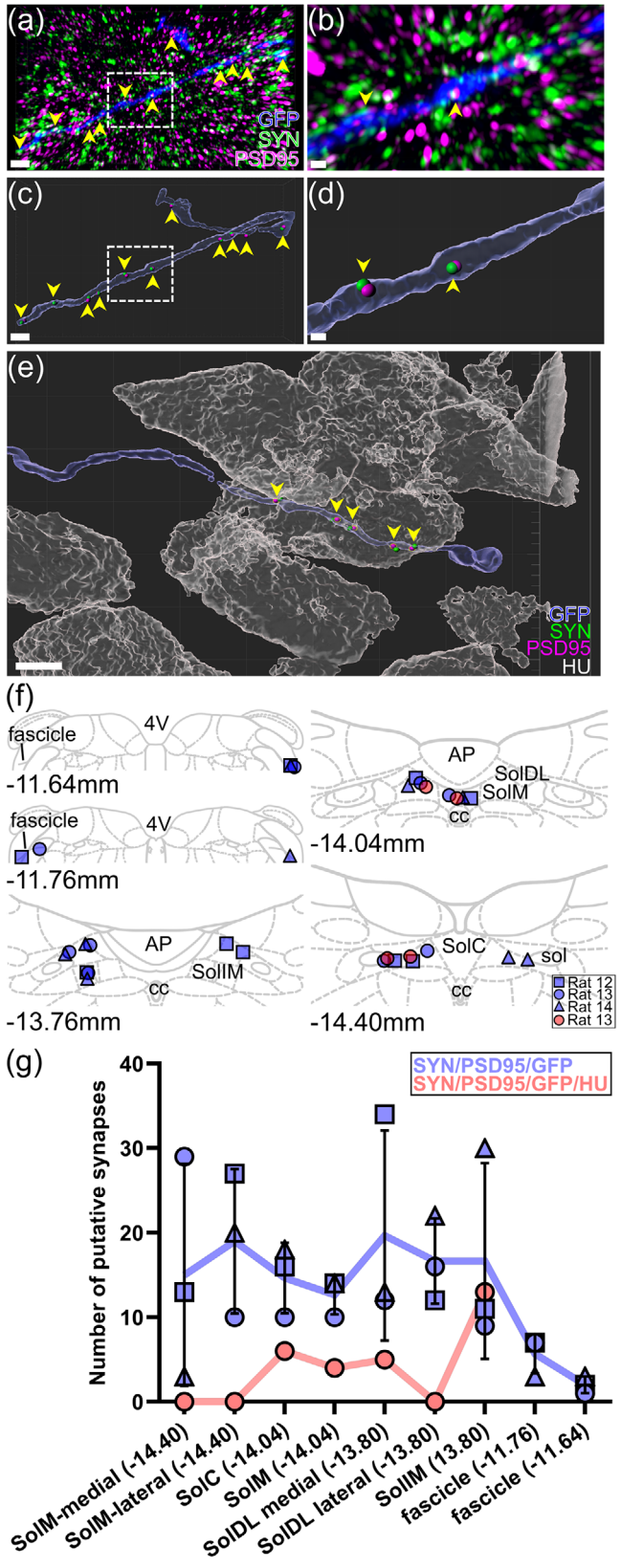

FIGURE 13 Quantification of putative synaptic contacts of vagal afferent axons within the nucleus of the solitary tract (NTS). (a) A confocal photomicrograph showing a vagal afferent from the stomach in blue, and immunoreactivity for the presynaptic marker synapsin-1 (SYN, green) and postsynaptic marker PSD-95 (magenta). The region

(Continues)

FIGURE 13 (Continued)
outlined with a dotted yellow box is shown in higher magnification (b). Imaris software was used to render a 3D surface of the vagal afferent axon (*blue*) and convert the putative synaptic puncta into "spots" (presynaptic, green; postsynaptic, magenta) and a snapshot view shown in (c). Putative synapses, defined as an overlapping pair of pre- and postsynaptic "spots" in close proximity to the surface of an afferent axon, are highlighted by the yellow arrowheads. A higher magnification view of the dotted boxed area in (c) is shown (d). The scale bar represents 2 μm (a, c) and 0.5 μm (b, d). Imaris software was also used to 3D surface render a vagal afferent axon (blue); a HU-immunoreactive NTS neuron (white); PSD95 (magenta); and synapsin (green) (e). Putative synapses, as defined in the Methods section and including close proximity between the afferent axon, pre- and postsynaptic markers, and the putative postsynaptic neurons, were identified and highlighted with yellow arrowheads. The scale bar represents 3 μm. The distribution of distribution of vagal afferent axons used for synapse quantification (purple, SYN/PSD-95/GFP, $n = 3$; red, SYN/PSD-95/GFP/HU, $n = 1$) were mapped onto schematic coronal brainstem sections (f). The number of putative synapses, quantified relative to NTS subnuclei/subregion, were counted, and are displayed in the graph (g). The purple data points represent close associations between pre- and postsynaptic proteins and a stomach vagal afferent ($n = 3$) whilst the red points represent close associations between both these elements at postsynaptic neurons ($n = 1$). Data are shown as individual values and, for the purple data, the line indicates mean ± *SD*. *Abbreviations*: AP, area postrema; cc, central canal; 4V, forth ventricle; sol, solitary tract; NTS subnuclei - SolDL, dorsolateral part; SolC, commissural part; SolM, medial part; SolIM, intermediate part

example, horseradish peroxidase based tracers inadequately label thin diameter axonal branches (Kubin, Kimura, & Davies, 1991). These factors may lead to differences in uptake of different tracers at sensory terminal endings in the same organ (Akgul Caglar et al., 2021; Saleeba, Dempsey, Le, Goodchild, & McMullan, 2019) and skew interpretations of results. Viral labeling also needs to be considered carefully with outcomes influenced by several factors, including tropism (Saleeba et al., 2019). In addition, differences in experimental animal species used needs to be considered (Kubin et al., 2006). A previous publication using the same serotype of AAVrg as that used in this study examined organ-specific vagal afferent labeling in mice (Han et al., 2018) and provided a different conclusion in relation to the distribution of afferents in the NTS. We do not have an explanation for this. Whilst the overall pattern is similar, some differences emerge from the use of channelrhodopsin2-fluorophores to examine distribution or different retrograde viruses, such as canine adenovirus, to transduce neurons. The rapid development of novel tools for examining neuronal anatomy and physiology is likely to generate interesting observations that will alter how we understand neuroanatomy in the coming years.

4.2 | Divergence of afferent input

Our conclusion that there is widespread divergent putative synaptic input from vagal viscerosensory neurons within the NTS is based upon transduction with two vectors inducing Cre expression in NDG

neurons projecting to a target organ and subsequent recombination and expression of synaptophysin. The observations were supported by immunohistochemical detection of synaptophysin in transduced neurons along with colocalization with a postsynaptic marker. We observed synaptophysin expression in axons within the vagal fascicles coursing from the dorso-lateral surface of the medulla to the st as well as within the st. Whilst the st does contain some neuronal somata, we conclude that synaptophysin may not accurately define synapses for anatomical classification, as the protein can be observed within the axon, *en route* to a synapse. We acknowledge that our understanding of synaptophysin expression in these neurons is limited, and that for example, it is not known if labeled synaptophysin is transported preferentially to different types of synapses, axo-axonal or *en passant* versus the classic terminal synapse (Holtmaat & Svoboda, 2009; X. Liu et al., 2021). Consequently, our synapse counting probably represents an underestimate, particularly as we also required coincident expression of the postsynaptic protein, PSD 95, to define a putative synapse.

4.3 | Selective afferent tropism

Using an AAV serotype with retrograde axonal transport properties we reliably and robustly transduced vagal sensory afferents following injection into their peripheral targets. We observed no evidence of transduction of vagal efferent neurons, either in the DMV or NAmb where their cell bodies are located, despite the high likelihood of injections being made in the region of their peripheral terminal fields. In some animals, we observed fluorescence in a very small number of axons in anatomical regions that might suggest transduction of vagal efferent neurons. However, we were never able to observe transduced somata, indicating that if transduced these neurons were very rare. It was in an attempt to transduce cardiac parasympathetic motor neurons that we initially targeted the atrial fat pads, but had no success, labeling only the afferents and intrinsic cardiac neurons (Figures 3 and 4). The reason why AAVrg appears to be selective for transduction of vagal sensory afferents is not clear but has been observed by others (Fontaine et al., 2021; Makhmutova et al., 2021). Interestingly one other study reports transduction of mouse efferent neurons with AAVrg following peripheral injections (Han et al., 2018), indicating a need to determine specificity for each application.

4.4 | Rare evidence for peripheral afferent collateralization

The intense labeling produced by our viral approach enabled us to observe that some NDG neurons innervate more than one peripheral organ. Whilst this was a rare observation it appears to be robust. Previous reports in rodents using DiI and CTB demonstrated that 7.4% of NDG neurons projected to both the stomach and the proximal duodenum (Zhong et al., 2008). The authors suggested this might contribute to poor spatial discrimination of visceral afferent sensory input. More recently two more publications have provided evidence of small numbers of colabeled NDG neurons projecting to different parts of the gastrointestinal tract (L. Bai et al., 2019; Muller et al., 2020).

5 | CONCLUSION

When injecting an AAV pseudotyped for retrograde transport into peripheral tissues we observed highly selective transduction of viscerosensory afferent neurons within the vagal system. We did not examine expression within the spinal sensory system. This enabled organ-specific labeling with fluorescent proteins and the observation of overlapping distributions of vagal afferent axons within the NTS, with little evidence of somatotopy. The pattern of labeling, which became very obvious in animals where only a very few neurons were transduced, showed extensive divergence throughout the NTS with substantial inputs to both the DMV and AP. This extensive axonal labeling following transduction corresponded to multiple putative synaptic inputs, as defined by immunohistochemistry for pre- and postsynaptic proteins, throughout different subnuclei of the NTS and to NTS neurons of different neurochemical phenotype. Convergent input from different organs to individual NTS neurons was also observed. The data indicate that an understanding of the organization of the NTS will likely require both organ and neurochemical characterization of the afferent in combination with the neurochemical phenotype and projection characteristics of the second-order neuron.

ACKNOWLEDGMENTS

Experiments were enabled by funding from the Australian National Health and Medical Research Council (APP#1163039 and #1156727) and the Australian Research Council (DP210102546).

All experiments were performed in male Sprague–Dawley rats (200-400g) in accordance with National Health & Medical Research Council of Australia guidelines; 2004 Australian code of practice for the Care and use of Animals for Scientific Purposes and 2008 Guidelines to Promote the Wellbeing of Animals Used for Scientific Purposes. All animal experiments were approved by University of Melbourne Animal Ethics Committee (Approval Number: 1613875, 1915005). All transgenic experiments were approved by the University of Melbourne Biosafety Committee (Approval Number: 2018/039) and certified by the Australian Government's Office of the Gene Technology Regulator. We gratefully acknowledge the assistance of Prof. John Furness (University of Melbourne) and Dr Alice McGovern (University of Melbourne) with the development of methods for injecting viruses into the stomach and trachea respectively. We also acknowledge the University of Melbourne, Biological Optical Microscopy Platform, and thank the staff for their expertise and technical assistance with microscopy, image processing and analysis. We thank Miss Meher Bassi for her assistance in generating the graphical abstract.

Open access publishing facilitated by The University of Melbourne, as part of the Wiley - The University of Melbourne agreement via the Council of Australian University Librarians.

AUTHOR CONTRIBUTIONS

J. K. B., S. Mc. D., and A. M. A. conceived and designed the experiments. J. K. B., D. G. S. F., A. A. C., A. B., and A. G. performed the experimental work. Y. L. and M. W. J. devised the LIMPID tissue clearing protocol. J. K. B. prepared the figures and, with S. Mc. D. and A. M. A., drafted the manuscript. J. K. B., A. A. C., M. R. M., S. Mc. D., and A. M. A. edited the manuscript and figures. A. M. A. provided overall supervision. All authors reviewed the results and provided important scientific feedback to the manuscript.

CONFLICT OF INTEREST

The authors do not report any conflicts of interests.

DATA AVAILABILITY STATEMENT

The data that support the findings of this study are available from the corresponding author upon reasonable request.

PEER REVIEW

The peer review history for this article is available at: https://publons.com/publon/10.1002/cne.25398.

ORCID

Jaspreet K. Bassi https://orcid.org/0000-0002-4397-9277
Anahita Ghanbari https://orcid.org/0000-0002-8364-6266
Stuart J. McDougall https://orcid.org/0000-0002-8778-675X
Andrew M. Allen https://orcid.org/0000-0002-2183-5360

REFERENCES

Adibi, M. (2019). Whisker-mediated touch system in rodents: From neuron to behavior. *Front Syst Neurosci*, *13*, 40. https://doi.org/10.3389/fnsys.2019.00040

Akgul Caglar, T., Durdu, Z. B., Turhan, M. U., Gunal, M. Y., Aydin, M. S., Ozturk, G., & Cagavi, E. (2021). Evaluation of the bilateral cardiac afferent distribution at the spinal and vagal ganglia by retrograde labeling. *Brain Research*, *1751*, 147201. https://doi.org/10.1016/j.brainres.2020.147201

Allen, A. M., O'Callaghan, E. L., Hazelwood, L., Germain, S., Castrop, H., Schnermann, J., & Bassi, J. K. (2008). Distribution of cells expressing human renin-promoter activity in the brain of a transgenic mouse. *Brain Research*, *1243*, 78–85. https://doi.org/10.1016/j.brainres.2008.09.046

Altschuler, S. M., Bao, X. M., Bieger, D., Hopkins, D. A., & Miselis, R. R. (1989). Viscerotopic representation of the upper alimentary tract in the rat: Sensory ganglia and nuclei of the solitary and spinal trigeminal tracts. *Journal of Comparative Neurology*, *283*(2), 248–268. https://doi.org/10.1002/cne.902830207

Andresen, M. C., & Paton, J. F. R. (2011). The nucleus of the solitary tract: Processing information from viscerosensory afferents. In Llewellyn-Smith, I. J. & Verberne, A. J. M. (Eds.), *Central Regulation of Autonomic Functions*. Oxford, U.K: Oxford University Press.

Bai, L., Mesgarzadeh, S., Ramesh, K. S., Huey, E. L., Liu, Y., Gray, L. A., Aitken, T. J., Chen, Y., Beutler, L. R., Ahn, J. S., Madisen, L., Zeng, H., Krasnow, M. A., & Knight, Z. A. (2019). Genetic identification of vagal sensory neurons that control feeding. *Cell*, *179*(5), 1129–1143. e1123. https://doi.org/10.1016/j.cell.2019.10.031

Bai, Y., Chen, Y. B., Qiu, X. T., Chen, Y. B., Ma, L. T., Li, Y. Q., Sun, H.-K., Zhang, M.-M., Zhang, T., Chen, T., Fan, B.-Y., Li, H., & Li, Y. Q. (2019). Nucleus tractus solitarius mediates hyperalgesia induced by chronic pancreatitis in rats. *World Journal of Gastroenterology*, *25*(40), 6077–6093. https://doi.org/10.3748/wjg.v25.i40.6077

Bailey, T. W., Hermes, S. M., Andresen, M. C., & Aicher, S. A. (2006). Cranial visceral afferent pathways through the nucleus of the solitary tract to caudal ventrolateral medulla or paraventricular hypothalamus: Target-specific synaptic reliability and convergence patterns. *Journal of Neuroscience*, *26*(46), 11893–11902. https://doi.org/10.1523/JNEUROSCI.2044-06.2006

Baluk, P., & Gabella, G. (1991). Afferent nerve endings in the tracheal muscle of guinea-pigs and rats. *Anatomy and Embryology*, *183*(1), 81–87. https://doi.org/10.1007/BF00185838

Berthoud, H. R., & Neuhuber, W. L. (2000). Functional and chemical anatomy of the afferent vagal system. *Autonomic Neuroscience*, *85*(1-3), 1–17. https://doi.org/10.1016/S1566-0702(00)00215-0

Berthoud, H. R., & Powley, T. L. (1992). Vagal afferent innervation of the rat fundic stomach: Morphological characterization of the gastric tension receptor. *Journal of Comparative Neurology*, *319*(2), 261–276. https://doi.org/10.1002/cne.903190206

Bertran-Gonzalez, J., Laurent, V., Chieng, B. C., Christie, M. J., & Balleine, B. W. (2013). Learning-related translocation of delta-opioid receptors on ventral striatal cholinergic interneurons mediates choice between goal-directed actions. *Journal of Neuroscience*, *33*(41), 16060–16071. https://doi.org/10.1523/JNEUROSCI.1927-13.2013

Bochorishvili, G., Nguyen, T., Coates, M. B., Viar, K. E., Stornetta, R. L., & Guyenet, P. G. (2014). The orexinergic neurons receive synaptic input from C1 cells in rats. *Journal of Comparative Neurology*, *522*(17), 3834–3846. https://doi.org/10.1002/cne.23643

Bonham, A. C., & Hasser, E. M. (1993). Area postrema and aortic or vagal afferents converge to excite cells in nucleus tractus solitarius. *American Journal of Physiology*, *264*(5 Pt 2), H1674–1685. https://doi.org/10.1152/ajpheart.1993.264.5.H1674

Borgmann, D., Ciglieri, E., Biglari, N., Brandt, C., Cremer, A. L., Backes, H., Tittgemeyer, M., Wunderlich, F. T., Brüning, J. C., & Fenselau, H. (2021). Gut-brain communication by distinct sensory neurons differently controls feeding and glucose metabolism. *Cell metabolism*, *33*(7), 1466–1482. e1467. https://doi.org/10.1016/j.cmet.2021.05.002

Card, J. P., Johnson, A. L., Llewellyn-Smith, I. J., Zheng, H., Anand, R., Brierley, D. I., Trapp, S., & Rinaman, L. (2018). GLP-1 neurons form a local synaptic circuit within the rodent nucleus of the solitary tract. *Journal of Comparative Neurology*, *526*(14), 2149–2164. https://doi.org/10.1002/cne.24482

Carter, D. A., Choong, Y. T., Connelly, A. A., Bassi, J. K., Hunter, N. O., Thongsepee, N., Llewellyn-Smith, I. J., Fong, A. Y., McDougall, S. J., & Allen, A. M. (2017). Functional and neurochemical characterization of angiotensin type 1A receptor-expressing neurons in the nucleus of the solitary tract of the mouse. *American Journal of Physiology. Regulatory, Integrative and Comparative Physiology*, *313*(4), R438–R449. https://doi.org/10.1152/ajpregu.00168.2017

Cechetto, D. F. (1987). Central representation of visceral function. *Federation Proceedings*, *46*(1), 17–23.

Chan, R. K., & Sawchenko, P. E. (1994). Spatially and temporally differentiated patterns of c-fos expression in brainstem catecholaminergic cell groups induced by cardiovascular challenges in the rat. *Journal of Comparative Neurology*, *348*(3), 433–460. https://doi.org/10.1002/cne.903480309

Chen, D., Bassi, J. K., Walther, T., Thomas, W. G., & Allen, A. M. (2010). Expression of angiotensin type 1A receptors in C1 neurons restores the sympathoexcitation to angiotensin in the rostral ventrolateral medulla of angiotensin type 1A knockout mice. *Hypertension*, *56*(1), 143–150. https://doi.org/10.1161/HYPERTENSIONAHA.110.151704

Chen, J., Cheng, M., Wang, L., Zhang, L., Xu, D., Cao, P., Wang, F., Herzog, H., Song, S., & Zhan, C. (2020). A vagal-NTS neural pathway that stimulates feeding. *Current Biology*, *30*(20), 3986–3998. e3985. https://doi.org/10.1016/j.cub.2020.07.084

Chi, J., Wu, Z., Choi, C. H. J., Nguyen, L., Tegegne, S., Ackerman, S. E., Crane, A., Marchildon, F., Tessier-Lavigne, M., & Cohen, P. (2018). Three-dimensional adipose tissue imaging reveals regional variation in beige fat biogenesis and PRDM16-dependent sympathetic neurite density. *Cell*

Metabolism, *27*(1), 226–236. e223. https://doi.org/10.1016/j.cmet.2017.12.011

Corbett, E. K., Sinfield, J. K., McWilliam, P. N., Deuchars, J., & Batten, T. F. (2005). Differential expression of vesicular glutamate transporters by vagal afferent terminals in rat nucleus of the solitary tract: Projections from the heart preferentially express vesicular glutamate transporter 1. *Neuroscience*, *135*(1), 133–145. https://doi.org/10.1016/j.neuroscience.2005.06.010

de Lartigue, G. (2014). Putative roles of neuropeptides in vagal afferent signaling. *Physiology & Behavior*, *136*, 155–169. https://doi.org/10.1016/j.physbeh.2014.03.011

Donoghue, S., Felder, R. B., Gilbey, M. P., Jordan, D., & Spyer, K. M. (1985). Post-synaptic activity evoked in the nucleus tractus solitarius by carotid sinus and aortic nerve afferents in the cat. *Journal of Physiology*, *360*, 261–273. https://doi.org/10.1113/jphysiol.1985.sp015616

Edwards, C. M., Strother, J., Zheng, H., & Rinaman, L. (2019). Amphetamine-induced activation of neurons within the rat nucleus of the solitary tract. *Physiology & Behavior*, *204*, 355–363. https://doi.org/10.1016/j.physbeh.2019.02.040

Fontaine, A. K., Futia, G. L., Rajendran, P. S., Littich, S. F., Mizoguchi, N., Shivkumar, K., Ardell, J. L., Restrepo, D., Caldwell, J. H., Gibson, E. A., & Weir, R. F. F. (2021). Optical vagus nerve modulation of heart and respiration via heart-injected retrograde AAV. *Science Reports*, *11*(1), 3664. https://doi.org/10.1038/s41598-021-83280-3

Fox, E. A., Phillips, R. J., Martinson, F. A., Baronowsky, E. A., & Powley, T. L. (2000). Vagal afferent innervation of smooth muscle in the stomach and duodenum of the mouse: Morphology and topography. *Journal of Comparative Neurology*, *428*(3), 558–576. https://doi.org/10.1002/1096-9861(20001218)428:3<558::aid-cne11>3.0.co;2-m

Fryscak, T., Zenker, W., & Kantner, D. (1984). Afferent and efferent innervation of the rat esophagus. A tracing study with horseradish peroxidase and nuclear yellow. *Anatomy and Embryology*, *170*(1), 63–70. https://doi.org/10.1007/BF00319459

Gaykema, R. P., Daniels, T. E., Shapiro, N. J., Thacker, G. C., Park, S. M., & Goehler, L. E. (2009). Immune challenge and satiety-related activation of both distinct and overlapping neuronal populations in the brainstem indicate parallel pathways for viscerosensory signaling. *Brain Research*, *1294*, 61–79. https://doi.org/10.1016/j.brainres.2009.07.076

Geerling, J. C., Kawata, M., & Loewy, A. D. (2006). Aldosterone-sensitive neurons in the rat central nervous system. *Journal of Comparative Neurology*, *494*(3), 515–527. https://doi.org/10.1002/cne.20808

Han, W., Tellez, L. A., Perkins, M. H., Perez, I. O., Qu, T., Ferreira, J., Ferreira, T. L., Quinn, D., Liu, Z.-W., Gao, X.-B., Kaelberer, M. M., Bohórquez, D. V., Shammah-Lagnado, S. J., de Lartigue, G., & de Araujo, I. E. (2018). A neural circuit for gut-induced reward. *Cell*, *175*(3), 665–678. e623. https://doi.org/10.1016/j.cell.2018.08.049

Hanamori, T., Kunitake, T., Kato, K., & Kannan, H. (1998). Neurons in the posterior insular cortex are responsive to gustatory stimulation of the pharyngolarynx, baroreceptor and chemoreceptor stimulation, and tail pinch in rats. *Brain Research*, *785*(1), 97–106. https://doi.org/10.1016/s0006-8993(97)01392-9

Hermes, S. M., Colbert, J. F., & Aicher, S. A. (2014). Differential content of vesicular glutamate transporters in subsets of vagal afferents projecting to the nucleus tractus solitarii in the rat. *Journal of Comparative Neurology*, *522*(3), 642–653. https://doi.org/10.1002/cne.23438

Herrity, A. N., Rau, K. K., Petruska, J. C., Stirling, D. P., & Hubscher, C. H. (2014). Identification of bladder and colon afferents in the nodose ganglia of male rats. *Journal of Comparative Neurology*, *522*(16), 3667–3682. https://doi.org/10.1002/cne.23629

Holtmaat, A., & Svoboda, K. (2009). Experience-dependent structural synaptic plasticity in the mammalian brain. *Nature Reviews Neuroscience*, *10*(9), 647–658. https://doi.org/10.1038/nrn2699

Hunter, D. D., & Undem, B. J. (1999). Identification and substance P content of vagal afferent neurons innervating the epithelium of the guinea pig trachea. *American Journal of Respiratory and Critical Care Medicine*, *159*(6), 1943–1948. https://doi.org/10.1164/ajrccm.159.6.9808078

Janig, W., & Habler, H. J. (2002). [Physiology and pathophysiology of visceral pain]. *Schmerz (Berlin, Germany)*, *16*(6), 429–446. https://doi.org/10.1007/s00482-002-0187-5

Kalia, M., & Richter, D. (1985). Morphology of physiologically identified slowly adapting lung stretch receptor afferents stained with intra-axonal horseradish peroxidase in the nucleus of the tractus solitarius of the cat. I. A light microscopic analysis. *Journal of Comparative Neurology*, *241*(4), 503–520. https://doi.org/10.1002/cne.902410409

Kalia, M., & Richter, D. (1988). Rapidly adapting pulmonary receptor afferents: I. Arborization in the nucleus of the tractus solitarius. *Journal of Comparative Neurology*, *274*(4), 560–573. https://doi.org/10.1002/cne.902740406

Kim, S. H., Hadley, S. H., Maddison, M., Patil, M., Cha, B., Kollarik, M., & Taylor-Clark, T. E. (2020). Mapping of sensory nerve subsets within the vagal ganglia and the brainstem using reporter mice for Pirt, TRPV1, 5-HT3, and Tac1 expression. *eNeuro*, *7*(2). https://doi.org/10.1523/ENEURO.0494-19.2020

Kubin, L., Alheid, G. F., Zuperku, E. J., & McCrimmon, D. R. (2006). Central pathways of pulmonary and lower airway vagal afferents. *Journal of Applied Physiology (1985)*, *101*(2), 618–627. https://doi.org/10.1152/japplphysiol.00252.2006

Kubin, L., Kimura, H., & Davies, R. O. (1991). The medullary projections of afferent bronchopulmonary C fibres in the cat as shown by antidromic mapping. *Journal of Physiology*, *435*, 207–228. https://doi.org/10.1113/jphysiol.1991.sp018506

Kupari, J., Haring, M., Agirre, E., Castelo-Branco, G., & Ernfors, P. (2019). An atlas of vagal sensory neurons and their molecular specialization. *Cell reports*, *27*(8), 2508–2523. e2504. https://doi.org/10.1016/j.celrep.2019.04.096

Li, Y., Serwanski, D. R., Miralles, C. P., Fiondella, C. G., Loturco, J. J., Rubio, M. E., & De Blas, A. L. (2010). Synaptic and nonsynaptic localization of protocadherin-gammaC5 in the rat brain. *Journal of Comparative Neurology*, *518*(17), 3439–3463. https://doi.org/10.1002/cne.22390

Liu, X., Yeo, S. H., McQuillan, H. J., Herde, M. K., Hessler, S., Cheong, I., Porteous, R., & Herbison, A. E. (2021). Highly redundant neuropeptide volume co-transmission underlying episodic activation of the GnRH neuron dendron. Elife, *10*. https://doi.org/10.7554/eLife.62455

Liu, Y., Watanabe, M., Rollins, A., & Jenkins, M. (2018). *Simple lipid-preserving optical clearing for fluorescent imaging (Conference Presentation)* (Vol. 10499): SPIE. https://doi.org/10.1117/12.2291174

Mahn, M., Prigge, M., Ron, S., Levy, R., & Yizhar, O. (2016). Biophysical constraints of optogenetic inhibition at presynaptic terminals. *Nature Neuroscience*, *19*(4), 554–556. https://doi.org/10.1038/nn.4266

Makhmutova, M., Weitz, J., Tamayo, A., Pereira, E., Boulina, M., Almaca, J., Rodriguez-Diaz, R., & Caicedo, A. (2021). Pancreatic beta-cells communicate with vagal sensory neurons. *Gastroenterology*, *160*(3), 875–888. e811. https://doi.org/10.1053/j.gastro.2020.10.034

Mazzone, S. B., Tian, L., Moe, A. A. K., Trewella, M. W., Ritchie, M. E., & McGovern, A. E. (2020). Transcriptional profiling of individual airway projecting vagal sensory neurons. *Molecular Neurobiology*, *57*(2), 949–963. https://doi.org/10.1007/s12035-019-01782-8

Mazzone, S. B., & Undem, B. J. (2016). Vagal afferent innervation of the airways in health and disease. *Physiological Reviews*, *96*(3), 975–1024. https://doi.org/10.1152/physrev.00039.2015

McDougall, S. J., Guo, H., & Andresen, M. C. (2017). Dedicated C-fibre viscerosensory pathways to central nucleus of the amygdala. *Journal of Physiology*, *595*(3), 901–917. https://doi.org/10.1113/JP272898

McDougall, S. J., Peters, J. H., & Andresen, M. C. (2009). Convergence of cranial visceral afferents within the solitary tract nucleus. *Journal of Neuroscience*, *29*(41), 12886–12895. https://doi.org/10.1523/JNEUROSCI.3491-09.2009

McGovern, A. E., Driessen, A. K., Simmons, D. G., Powell, J., Davis-Poynter, N., Farrell, M. J., & Mazzone, S. B. (2015). Distinct brainstem and

forebrain circuits receiving tracheal sensory neuron inputs revealed using a novel conditional anterograde transsynaptic viral tracing system. *Journal of Neuroscience*, *35*(18), 7041–7055. https://doi.org/10.1523/JNEUROSCI.5128-14.2015

Menuet, C., Connelly, A. A., Bassi, J. K., Melo, M. R., Le, S., Kamar, J., Kumar, N. N., McDougall, S. J., McMullan, S., & Allen, A. M. (2020). PreBotzinger complex neurons drive respiratory modulation of blood pressure and heart rate. Elife, *9*. https://doi.org/10.7554/eLife.57288

Menuet, C., Le, S., Dempsey, B., Connelly, A. A., Kamar, J. L., Jancovski, N., Bassi, J. K., Walters, K., Simms, A. E., Hammond, A., Fong, A. Y., Goodchild, A. K., McMullan, S., & Allen, A. M. (2017). Excessive respiratory modulation of blood pressure triggers hypertension. *Cell metabolism*, *25*(3), 739–748. https://doi.org/10.1016/j.cmet.2017.01.019

Mifflin, S. W. (1996). Convergent carotid sinus nerve and superior laryngeal nerve afferent inputs to neurons in the NTS. *American Journal of Physiology*, *271*(4 Pt 2), R870–880. https://doi.org/10.1152/ajpregu.1996.271.4.R870

Mifflin, S. W., & Felder, R. B. (1990). Synaptic mechanisms regulating cardiovascular afferent inputs to solitary tract nucleus. *American Journal of Physiology*, *259*(3 Pt 2), H653–661. https://doi.org/10.1152/ajpheart.1990.259.3.H653

Muller, P. A., Schneeberger, M., Matheis, F., Wang, P., Kerner, Z., Ilanges, A., Pellegrino, K., del Mármol, J., Castro, T. B. R., Furuichi, M., Perkins, M., Han, W., Rao, A., Pickard, A. J., Cross, J. R., Honda, K., de Araujo, I., & Mucida, D. (2020). Microbiota modulate sympathetic neurons via a gut-brain circuit. *Nature*, *583*(7816), 441–446. https://doi.org/10.1038/s41586-020-2474-7

Ngo, H. B., Melo, M. R., Layfield, S., Connelly, A. A., Bassi, J. K., Xie, L., Menuet, C., McDougall, S. J., Bathgate, R. A. D., & Allen, A. M. (2020). A chemogenetic tool that enables functional neural circuit analysis. *Cell reports*, *32*(11), 108139. https://doi.org/10.1016/j.celrep.2020.108139

Ootani, S., Umezaki, T., Shin, T., & Murata, Y. (1995). Convergence of afferents from the SLN and GPN in cat medullary swallowing neurons. *Brain Research Bulletin*, *37*(4), 397–404. https://doi.org/10.1016/0361-9230(95)00018-6

Paintal, A. S. (1973). Vagal sensory receptors and their reflex effects. *Physiological Reviews*, *53*(1), 159–227. https://doi.org/10.1152/physrev.1973.53.1.159

Paton, J. F. (1998). Pattern of cardiorespiratory afferent convergence to solitary tract neurons driven by pulmonary vagal C-fiber stimulation in the mouse. *Journal of Neurophysiology*, *79*(5), 2365–2373. https://doi.org/10.1152/jn.1998.79.5.2365

Paton, J. F., Li, Y. W., Deuchars, J., & Kasparov, S. (2000). Properties of solitary tract neurons receiving inputs from the sub-diaphragmatic vagus nerve. *Neuroscience*, *95*(1), 141–153. https://doi.org/10.1016/s0306-4522(99)00416-9

Paxinos, G., & Watson, C. (2004). *The Rat Brain in Stereotaxic Coordinates* (5 ed.): Academic Press.

Peters, J. H., McDougall, S. J., Fawley, J. A., & Andresen, M. C. (2011). TRPV1 marks synaptic segregation of multiple convergent afferents at the rat medial solitary tract nucleus. *PLoS One*, *6*(9), e25015. https://doi.org/10.1371/journal.pone.0025015

Powley, T. L., Jaffey, D. M., McAdams, J., Baronowsky, E. A., Black, D., Chesney, L., Evans, C., & Phillips, R. J. (2019). Vagal innervation of the stomach reassessed: Brain-gut connectome uses smart terminals. *Ann N Y Acad Sci*, *1454*(1), 14–30. https://doi.org/10.1111/nyas.14138

Prescott, S. L., Umans, B. D., Williams, E. K., Brust, R. D., & Liberles, S. D. (2020). An airway protection program revealed by sweeping genetic control of vagal afferents. *Cell*, *181*(3), 574–589. e514. https://doi.org/10.1016/j.cell.2020.03.004

Renier, N., Wu, Z., Simon, D. J., Yang, J., Ariel, P., & Tessier-Lavigne, M. (2014). iDISCO: A simple, rapid method to immunolabel large tissue samples for volume imaging. *Cell*, *159*(4), 896–910. https://doi.org/10.1016/j.cell.2014.10.010

Saleeba, C., Dempsey, B., Le, S., Goodchild, A., & McMullan, S. (2019). A student's guide to neural circuit tracing. *Front Neurosci*, *13*, 897. https://doi.org/10.3389/fnins.2019.00897

Saper, C. B. (2002). The central autonomic nervous system: Conscious visceral perception and autonomic pattern generation. *Annual Review of Neuroscience*, *25*, 433–469. https://doi.org/10.1146/annurev.neuro.25.032502.111311

Sauerbeck, A. D., Gangolli, M., Reitz, S. J., Salyards, M. H., Kim, S. H., Hemingway, C., Gratuze, M., Makkapati, T., Kerschensteiner, M., Holtzman, D. M., Brody, D. L., & Kummer, T. T. (2020). SEQUIN multiscale imaging of mammalian central synapses reveals loss of synaptic connectivity resulting from diffuse traumatic brain injury. *Neuron*, *107*(2), 257–273. e255. https://doi.org/10.1016/j.neuron.2020.04.012

Schatzle, P., Wuttke, R., Ziegler, U., & Sonderegger, P. (2012). Automated quantification of synapses by fluorescence microscopy. *Journal of Neuroscience Methods*, *204*(1), 144–149. https://doi.org/10.1016/j.jneumeth.2011.11.010

Sevigny, C. P., Bassi, J., Williams, D. A., Anderson, C. R., Thomas, W. G., & Allen, A. M. (2012). Efferent projections of C3 adrenergic neurons in the rat central nervous system. *Journal of Comparative Neurology*, *520*(11), 2352–2368. https://doi.org/10.1002/cne.23041

Shapiro, R. E., & Miselis, R. R. (1985). The central organization of the vagus nerve innervating the stomach of the rat. *Journal of Comparative Neurology*, *238*(4), 473–488. https://doi.org/10.1002/cne.902380411

Shin, J. W., & Loewy, A. D. (2009). Gastric afferents project to the aldosterone-sensitive HSD2 neurons of the NTS. *Brain Research*, *1301*, 34–43. https://doi.org/10.1016/j.brainres.2009.08.098

Tervo, D. G., Hwang, B. Y., Viswanathan, S., Gaj, T., Lavzin, M., Ritola, K. D., Lindo, S., Michael, S., Kuleshova, E., Ojala, D., Huang, C.-C., Gerfen, C. R., Schiller, J., Dudman, J. T., Hantman, A. W., Looger, L. L., Schaffer, D. V., & Karpova, A. Y. (2016). A designer AAV variant permits efficient retrograde access to projection neurons. *Neuron*, *92*(2), 372–382. https://doi.org/10.1016/j.neuron.2016.09.021

Wang, Y. B., de Lartigue, G., & Page, A. J. (2020). Dissecting the role of subtypes of gastrointestinal vagal afferents. *Front Physiol*, *11*, 643. https://doi.org/10.3389/fphys.2020.00643

Williams, E. K., Chang, R. B., Strochlic, D. E., Umans, B. D., Lowell, B. B., & Liberles, S. D. (2016). Sensory neurons that detect stretch and nutrients in the digestive system. *Cell*, *166*(1), 209–221. https://doi.org/10.1016/j.cell.2016.05.011

Zhao, Q., Yu, C. D., Wang, R., Xu, Q. J., Pra, R. D., Zhang, L., & Chang, R. B. (2022). A multidimensional coding architecture of the vagal interoceptive system. *Nature*, 603(7901). doi:https://doi.org/10.1038/s41586-022-04515-5

Zhong, F., Christianson, J. A., Davis, B. M., & Bielefeldt, K. (2008). Dichotomizing axons in spinal and vagal afferents of the mouse stomach. *Digestive Diseases and Sciences*, *53*(1), 194–203. https://doi.org/10.1007/s10620-007-9843-z

How to cite this article: Bassi, J. K., Connelly, A. A., Butler, A. G., Liu, Y., Ghanbari, A., Farmer, D. G. S., Jenkins, M. W., Melo, M. R., McDougall, S. J., & Allen, A. M. (2022). Analysis of the distribution of vagal afferent projections from different peripheral organs to the nucleus of the solitary tract in rats. *Journal of Comparative Neurology*, *530*, 3072–3103. https://doi.org/10.1002/cne.25398